nature geoscience

SUPPLEMENTARY INFORMATION

https://doi.org/10.1038/s41561-018-0200-y

In the format provided by the authors and unedited.

Cenozoic record of $\delta^{34}S$ in foraminiferal calcite implies an early Eocene shift to deep-ocean sulfide burial

Victoria C. F. Rennie[1]*, Guillaume Paris[2,3], Alex L. Sessions[2], Sigal Abramovich[4], Alexandra V. Turchyn[1] and Jess F. Adkins[2]

[1]Department of Earth Sciences, University of Cambridge, Cambridge, UK. [2]Division of Geological and Planetary Sciences, California Institute of Technology, Pasadena, CA, USA. [3]Centre de Recherches Pétrographiques et Géochimiques, CRPG, UMR 7358, CNRS, Université de Lorraine, Vandoeuvre-lès-Nancy, France. [4]Department of Geological and Environmental Sciences, Ben Gurion University of the Negev, Beer Sheva, Israel. *e-mail: vcr22@cam.ac.uk

A novel Cenozoic record of seawater sulfur isotopes from foraminiferal calcite

Supplementary Material

1. Foraminiferal cleaning

Foraminiferal calcite is associated with several other phases that could contain sufficient sulfur to contaminate the measured CAS. Calcitic foraminiferal tests contain abundant associated organic matter, which foraminifera use to lay down a template for calcification[1]. This organic matter is likely to contain sulfur, typically at ~1% abundance, although its contribution to the overall sulfur concentration in foraminifera has been suggested to be small[2].

Sediments have other constituents that may contain sulfur, and which may be adhered onto the foraminiferal tests. These include exogenous organic molecules, clay minerals, recrystallized calcite, pyrite (from bacterial sulfate reduction), barite (from the water column, or precipitated within pore fluid), and ferromanganese crusts. If barite is adhered to the carbonate, its high sulfate content makes it likely to contaminate the overall CAS $\delta^{34}S$ value. Diagenetic barite forms as barium reacts with sulfate in pore fluid. Sources of barium into pore fluid include its in-situ release from remineralized organic matter and dissolving carbonates, or diffusion from below (pelagic, or seawater, barite dissolves when the pore fluid sulfate concentrations have dropped to zero). The sulfur content and associated $\delta^{34}S$ of ferromanganese crusts are less well known. Ferromanganese crusts form as iron and manganese are reduced at depth (coupled to the microbial oxidation of organic matter in the sediment column). Dissolved iron and manganese can diffuse upwards through the sediment, and precipitate as oxides in oxygenated parts of the sediment column. Ferro-manganese

oxides will coat sedimentary grains (including foraminiferal tests), and may incorporate trace concentrations of other elements, such as neodymium, and lead. It is not clear whether these coatings contain sulfur, but if this is the case then they could provide another source of contamination. Because of these possible contaminants, it becomes important to test which phases associated with foraminiferal tests in the sediment column contain sufficient sulfur to affect measured CAS $\delta^{34}S$ values.

The long history of geochemical research into foraminifera has resulted in the optimisation of methods to remove clays, (hydr)oxides, organics, ferromanganese crusts, and barite from samples of handpicked foraminifera. The methods used for this study are modified from[3,4] to account for larger sample sizes. Methods used to remove barite[5] were not used here because the methods employed strongly chelating cations, resulting in the dissolution of a significant proportion of calcite, as well as any barite (although barium concentrations were measured to look for possible contamination – see below). Implementing a barite removal step would triple the amount of calcite needed. Additionally, standard cleaning methods do not attempt to chemically remove pyrite[6], although in some cases microcrystalline pyrite can be oxidized during CAS extraction[7]. This is addressed by visually ensuring as much as possible that the samples do not contain pyrite, replacing all the oxidizing acids used (such as nitric acid) with non-oxidizing acids (such as hydrochloric acid), and dissolving samples in as weak an acid as possible.

2.1 Cleaning Tests and core-top results

The typical sequence for cleaning foraminiferal calcite for trace element work involves the sequential removal of clays, organic material (using an oxidizing solution) and oxidative coatings (using a reducing solution).

Samples were crushed between two glass plates. Samples for clay removal were then mixed with Aristar methanol and agitated in an ultrisonicator for 30 s, before removing the overlying fluid. This step was repeated twice with methanol and multiple times with 18.2 Milli-Q water until the agitated solution was clear. The samples were then inspected under the microscope for the manual removal of any visual contaminants. Samples undergoing oxidative cleaning were treated with 100 μl of ultraclean hydrogen peroxide in 10 ml of 0.1 M sodium hydroxide, in a water bath with ultrasonication for 10 minutes. Samples that were additionally reductively cleaned were initially treated with 100 μl hydrazine solution (250 μl hydrous hydrazine in 2 ml ammonium hydroxide and 2 ml 0.25 M citric acid/16 M ammonia solution) for 45 mins in a water bath, with intermittent ultrasonification. The final cleaning step test (steps 4 and 6) was a leaching step with 500 μl of 0.001 M HCl solution for 1 minute- half of the reductively cleaned samples and half of the reductively-then oxidatively cleaned samples (post steps 3&5) underwent leaching.

Four species (*G. siphonifera, O. universa, G. menardii, and G. sacculifer*) in the >250 μm size fraction were picked from the coarse fraction of the top 0.5 cm from WIND 10B in the Western Indian Ocean. Species were divided up into ~4 mg subsamples prior to crushing. Splitting the sample before crushing has one advantage over crushing the sample prior to splitting, because the final $\delta^{34}S$ will express the true variability expected from any given foraminiferal sample – both the intra-specific variability and any that is the result of different cleaning approaches. The

disadvantage of this method is that it tests for two sources of variability at once, and therefore cannot distinguish between them[8]. For the purposes of quantifying the total "external variability" in a sample, however, this method provides a more useful test.

Each 4 mg sample was treated with a variety of different cleaning steps, as outlined in Figure S.1. Where sample volume allowed, duplicate or triplicate samples were processed (for *O. universa*, and *G. menardii*), however, for other species with low sample volumes, some steps were omitted (e.g. steps 1, 3 and 5).

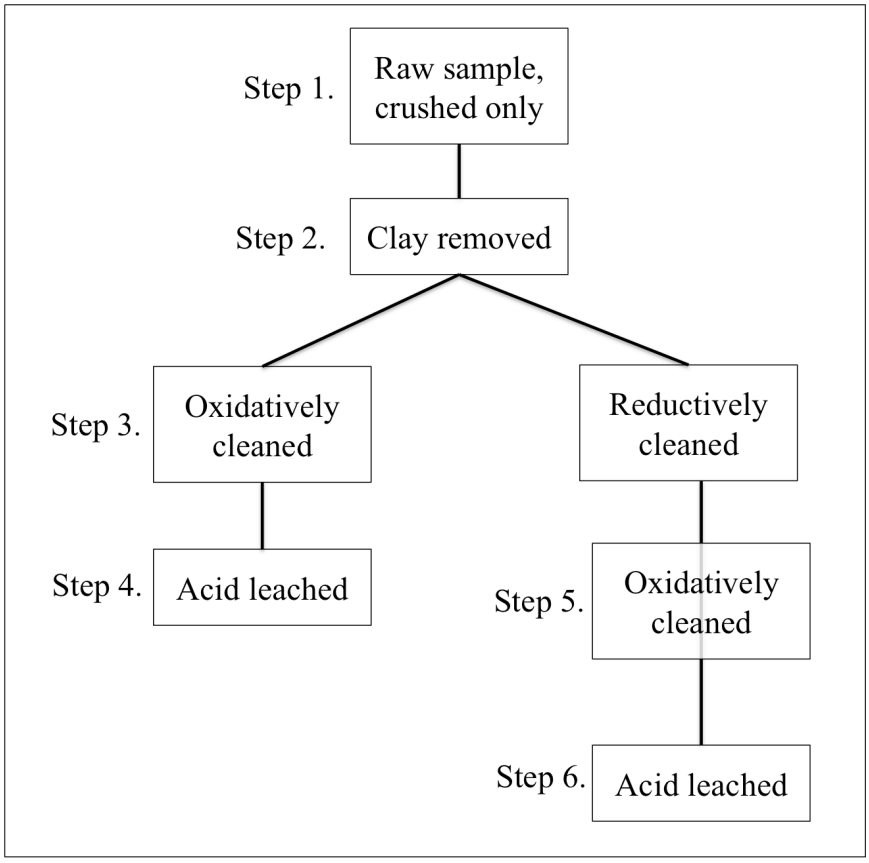

Figure S.1. Flow diagram of the cleaning steps for the cleaning test.

Samples were dissolved (in 0.2 M ultraclean HCl) prior to analysis, and an aliquot was run on the ICP-AES to determine calcium concentrations. Additionally, samples were run for the standard suite of trace elements: Ba/Ca, Fe/Ca, Mn/Ca by

ICP-AES. The natural abundance of these elements in Quaternary planktonic foraminifera is well known, due to the long-standing body of research into these microfossils. Any trace element concentration that is significantly higher than this natural variability indicates the likely presence of contaminants within the samples.

The use of trace element analysis by ICP-AES is also useful for the identification of ferro-manganese crusts (using Fe/Mn ratios as well as Fe/Ca and Mn/Ca ratios), clay contamination (using Al/Ca ratios) and glove/lab contamination (using Zn/Ca ratios- Zn is in very low concentrations in natural carbonate, but in high concentrations on surfaces and gloves in the laboratory).

The remaining solution was dried down in a laminar flow hood and redissolved in 0.2 M ultraclean HCl and then processed through columns after[2,9]. Each sample batch was run with a blank, and each column batch had at least one column with seawater (and for the long-term record, an additional consistency standard). Samples were analysed on a ThermoScientific Neptune Plus MC-ICP-MS using a desolvating membrane (Aridus, Cetac) at the California Institute of Technology, with sample-standard bracketing to correct for mass fractionation within the instrument[10] and reported relative to V-CDT. The V-CDT calibration was made using an in-house Na_2SO_4 standard using the absolute ratio measured previously[10]. With each batch of columns, we ran a seawater and a carbonate consistency standard consisting of a dissolved coral, modified by the addition (1%) of a pure calcium solution. Column seawater results were 21.01 ± 0.12‰, in agreement with previously published values[11] and carbonate consistency standards were 22.1 ± 0.3‰.

2.2 Results

The results of the cleaning test for the four species of core-top foraminifera (>250 μm) from WIND 10B in the Western Indian Ocean are displayed in Figure S.2. In three species (*G. menardii, O. universa* and *G. sacculifer*), the average $\delta^{34}S$ decreases from raw to clay removal to oxidatively cleaned samples (Steps 1-3), while reductively cleaned samples generally have the highest average $\delta^{34}S$. This is in contrast to samples of *G. siphonifera*, which has measured CAS $\delta^{34}S$ values for clay removed, oxidatively cleaned (leached) and reductively cleaned (leached) which are only 0.14‰ apart, similar to the analytical uncertainty for the Neptune MC-ICPMS

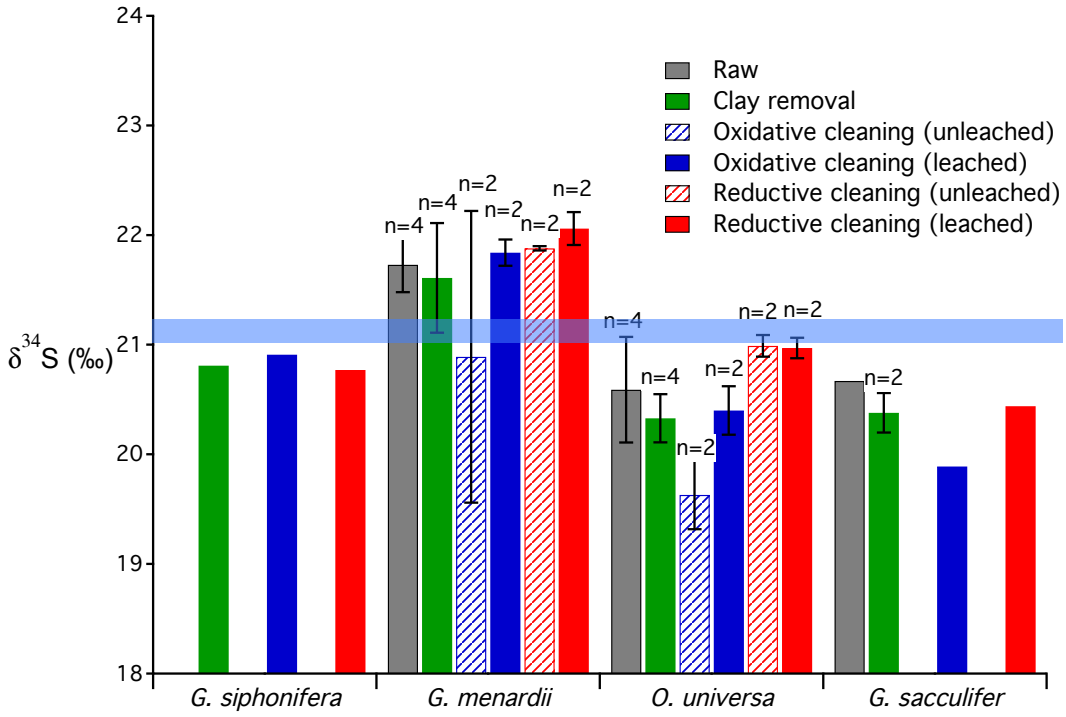

Figure S.2. $\delta^{34}S$ values for different species, subdivided by cleaning step. Where more than one sample was analyzed the average isotope composition is shown, along with the standard deviation (1σ) displayed as an error bar, and the number of samples analyzed. The blue horizontal bar represents seawater $\delta^{34}S$ (21.1‰).

Where more than one sample was analyzed, the standard deviation (1σ) of the results is reported as an error bar. The variability in $\delta^{34}S$ (as measured by the standard deviation) is higher across the first three steps (raw to oxidatively cleaned samples), than for the final three cleaning steps (oxidatively cleaned (leached) samples, and reductively cleaned samples- Steps 4-6). The reductively cleaned foraminifera had $\delta^{34}S$, which were closer to those expected for seawater, and there was lower variability between replicates. This suggests that reductively cleaning foraminifera removes more contaminants than the previous steps. This observation is unexpected because there are no known sulfur bearing phases in ferromanganese coatings. In general, while the oxidation of pyrite by HCl has been demonstrated[7], it appears that, for very small carbonate samples, this is not the case[6]. However, Fe^{3+} is an efficient oxidizing agent for pyrite, so perhaps the removal of this phase limits pyrite oxidation during the subsequent samples dissolution[12].

Three species (*G. siphonifera, O. universa,* and *G. sacculifer*) have a foraminiferal CAS $\delta^{34}S$ that is at or below the $\delta^{34}S$ of seawater. Reductively cleaned samples for these species have $\delta^{34}S$ values within 0.2−0.6‰ of seawater (21.1‰). This sulfur isotope composition is slightly higher than that expected for *O. universa* from culturing experiments, in which *O. universa* (which were only oxidatively cleaned) was shown to incorporate sulfate with a $\delta^{34}S$ value that was 1‰ lower than that of sulfate in the culturing media[2]. The sulfate concentrations in cultured *O. universa* are also twice as high as any sulfate concentrations in *O. universa* in this core-top. The difference between cultured and core-top *O. universa* are not easy to reconcile- although oxidatively cleaned samples in this study were also ~1‰ lower than reductively cleaned samples. If different cleaning methods have an impact on the

measured foraminiferal CAS $\delta^{34}S$ (as is suggested by this data), then to investigate real differences between cultured and core-top foraminifera, they must have been cleaned identically.

In contrast to the other foraminifera, *G. menardii* is 1‰ higher than the other samples, across all cleaning steps except Step 3 (oxidatively cleaned but unleached) with an average foraminiferal CAS $\delta^{34}S$ of 21.7‰ rather than of 19.9‰. The average CAS $\delta^{34}S$ value for reductively cleaned *G. menardii* is 22‰, 1‰ higher than the other species and modern seawater. This highlights the necessity of using single species foraminifera, and splicing different records of single species foraminifera in order to remove any offsets related to inter-species differences. The offsets related to inter-species differences in the $\delta^{34}S$ of calcite are possibly related to different biomineralization conditions within different foraminifera (e.g., rates and mechanisms of biomineralization, cellular conditions, presence/absence of symbionts[1]), however distinguishing the mechanism is beyond the scope of these data.

3. Sulfur isotope record

The sulfur isotope record was collected from six different, globally distributed core sites (see Figure S.3.).

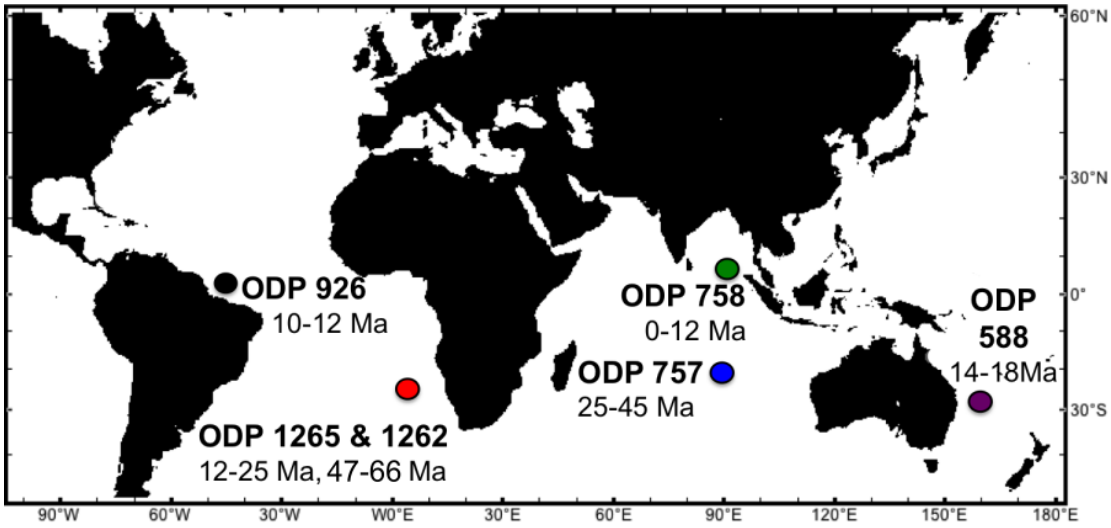

Figure S.3 - Map of the core-sites used to make the second Cenozoic record of foraminiferal CAS $\delta^{34}S$, labeled with the age intervals used for each site. Colored symbols on the map correspond to colors of the symbols used in Figure 1. Age models for DSDP 588, ODP 757, 758, 926, 1262 and 1265 were [13-19].

We addressed the likely sulfur isotope offset between species by comparing overlapping records of single species foraminifera, pinning the record to modern seawater values, using the offsets found in modern core-top samples (see Table S.1 for offset-corrected species).

Species	Species spliced to	$\delta^{34}S$ of offset
G. bulloides, praebulloides	*D. venezuelana*, 12Ma, 15Ma	+1‰
O. universa	*D. venezuelana* at 12Ma, modern cultures	+1‰
G. index	*D. galavisi,* 36 Ma, *Catapsydrax. U* 37 Ma	+0.7‰
A. bullbrooki	*G. index,* 45 Ma *M. aragonensis,* 47 Ma	+0.8‰
G. menardii	Core-top	-1‰

Table S.1 Species splicing offsets

Most overlapping foraminiferal samples had consistent $\delta^{34}S$ values. Only six species (see Table S.1- *G. bulloides & praebulloides*, *O. universa*, *G. index*, *A. bullbrooki*, and *G. menardii*) of foraminifera had measured CAS $\delta^{34}S$ values that were isotopically offset from overlapping sample of foraminiferal CAS $\delta^{34}S$. Isotopic offsets were determined by comparing the foraminiferal CAS $\delta^{34}S$ values from two different species picked out of the sample sediment horizon (and therefore from the same geological time interval, assuming that each sediment horizons represents a discrete time interval, and that bioturbation and sediment reworking are negligible relative to the residence time and sampling intervals associated with sulfate in the ocean.). Where two species co-exist in more than one time interval, the measured foraminiferal CAS $\delta^{34}S$ offset between them remained constant, engendering confidence in the values used for splicing single species records.

Certain features of the Cenozoic foraminiferal CAS $\delta^{34}S$ record appear to be confirmed independently by different foraminiferal species, for example, from 10 to 6 Ma there is a 1‰ decrease in foraminiferal CAS $\delta^{34}S$ both in *G. menardii* and in *D. venezuelana* across two different sites (758 and 926), and a similar offset between the two species at both time intervals. An additional example is from ~53 – 48 Ma, where three different foraminiferal species (*M. lensiformis*, *M. aragonensis*, and *M. caucascia*) all show steep increases in CAS $\delta^{34}S$, and where overlap exists between species there is a good match between each species' measured CAS $\delta^{34}S$.

4. Screening for possible contamination

Using the ICP-AES data, it is possible to rule out blank contamination by comparison

of the foraminiferal CAS $\delta^{34}S$ against total sulfate in each sample (see Figure S.4). There is no correlation between foraminiferal CAS $\delta^{34}S$ and total sulfate in the samples, as would be expected if a blank were present in varying amounts.

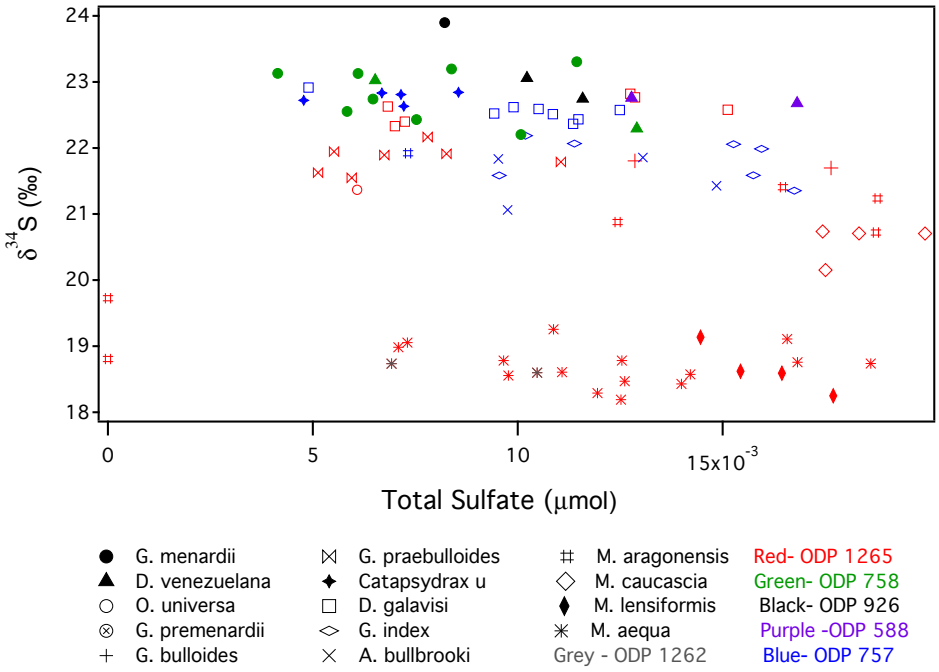

Figure S.4. - Foraminiferal CAS $\delta^{34}S$ (un-spliced) against total sulfate for the samples.

It is also possible to rule out barite contamination by comparing foraminiferal CAS $\delta^{34}S$ and sulfate concentrations against barium concentrations, and total sulfate in the sample against total barium in the sample (see Figure S.5). Neither foraminiferal CAS $\delta^{34}S$, SO_4/Ca ratios, or total sulfate in the samples show any relationship to either Ba/Ca or total barium in the samples, indicating that barite contamination, if any, is insignificant. The detection limit of Ba over the experimental runs was a maximum of 0.0001 ppm (results recorded below this concentration were assumed to be too poorly calibrated), which corresponded to a sub-sample volume of 10µl out of a total sample volume of 470 µl, or 1ng Ba. or 0.007 nmol. Any "unseen barium" would therefore

contribute a maximum sulfur contribution of 0.2 ng to a 5 ng sample, or ~5%.

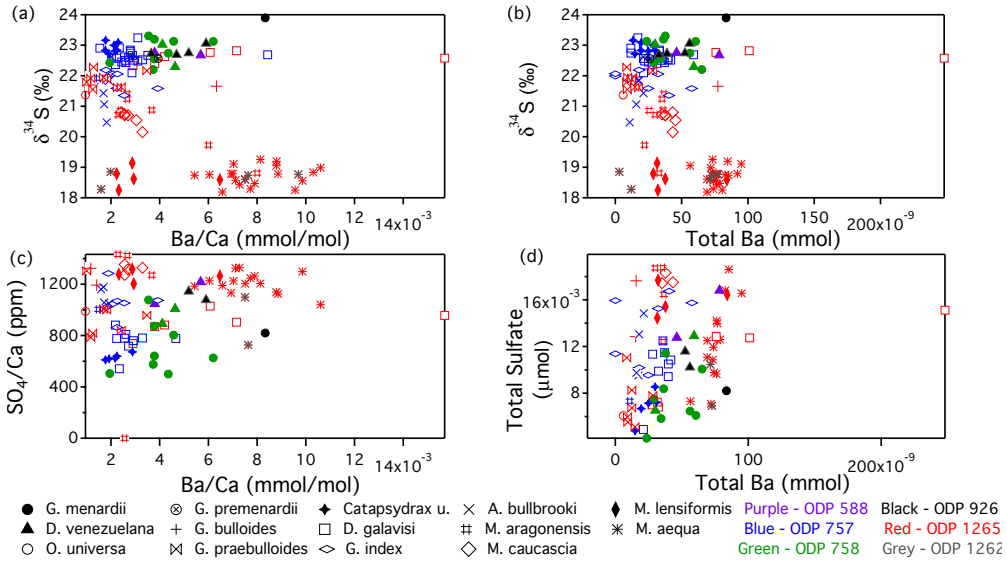

Figure S.5 - foraminiferal CAS $\delta^{34}S$ (un-spliced) against Ba/Ca (a) and Total barium (b), and sulfate/calcium ratios (un-spliced) against Ba/Ca (c), and total sulfate against total barium (d).

Iron concentration data (Figure S.6) also shows no correlation with $\delta^{34}S$, indicating that there is negligible pyrite contamination in the Cenozoic foraminiferal CAS samples. However, there does appear to be a correlation between total iron and foraminiferal CAS $\delta^{34}S$ for the *G. menardii* samples from Site 758, which spans the most recent 10 Ma. No such correlation is apparent between sulfate concentrations and iron concentrations, or total sulfate against total iron (See Figure S.6). This suggests that there could be an iron phase contributing to the measured foraminiferal CAS $\delta^{34}S$ of these samples, but not supplying sufficient sulfate to alter the sulfate concentration of the sample.

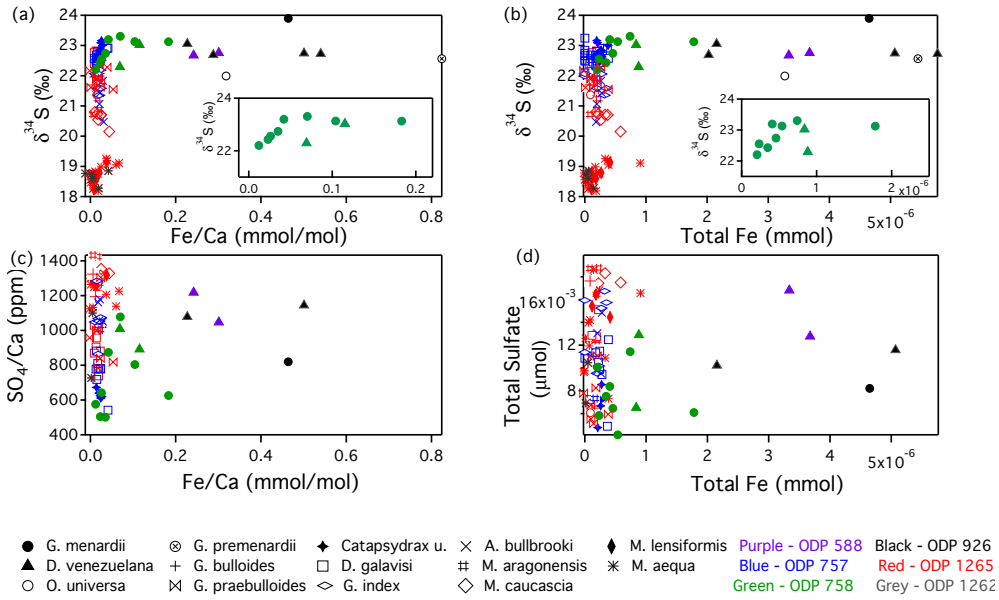

Figure S.6 - foraminiferal CAS $\delta^{34}S$ (un-spliced) against Fe/Ca (a) and Total iron (b), with a zoomed in view of Site 758 samples (see insets), and sulfate/calcium ratios (un-spliced) against Fe/Ca (c), and total sulfate against total iron (d).

A similar correlation between foraminiferal CAS $\delta^{34}S$ and total manganese in the *G. menardii* samples from Site 758 can be seen (see Figure S.7). There is also a correlation between sulfate concentrations and manganese concentrations/total manganese in these samples. Furthermore, there is a distinct correlation between iron and manganese concentrations for the Site 758 *G menardii* samples (see Figure S.8). The other foraminiferal samples analyzed for this Cenozoic record either have high manganese and high iron concentrations (likely ferro-manganese oxides), or high manganese and low iron concentrations (likely manganese carbonates), however these *G. menardii* samples have high manganese concentrations, with intermediate iron concentrations. This is therefore likely to be some form of manganese precipitate that is rich in both iron and sulfur, and has formed on foraminifera in contact with the pore fluid of this site. There are only two additional samples from Site 758 (both *D. venezuelana*), too few to confirm that the excess manganese is from a diagenetic

coating that impacts all foraminifera at this site. However these two *D. venezuelana* samples show a similar relationship between SO_4/Ca vs. Mn/Ca as the *G. menardii* samples at this site, which indicates that the *D. venezuelana* samples may also be contaminated by an Mn-rich phase in the sediments.

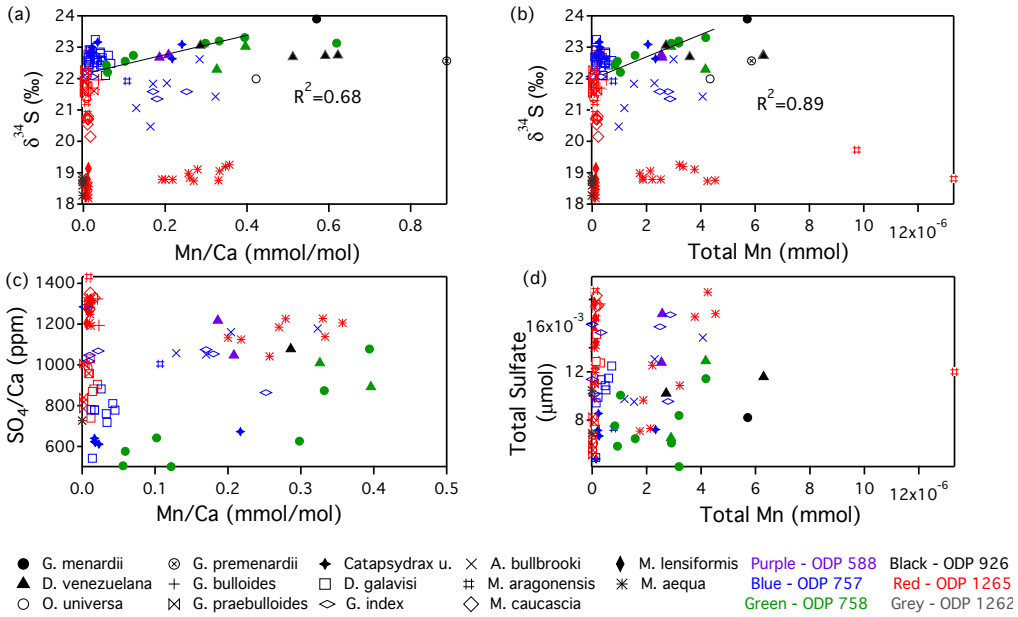

Figure S.7 - foraminiferal CAS δ^{34}S (un-spliced) against Mn/Ca (a) and Total manganese (b), and sulfate/calcium ratios (un-spliced) against Mn/Ca (c), and total sulfate against total manganese (d). R^2 values for best-fits for the *G. menardii* samples for Site 758 are displayed on the relevant graphs.

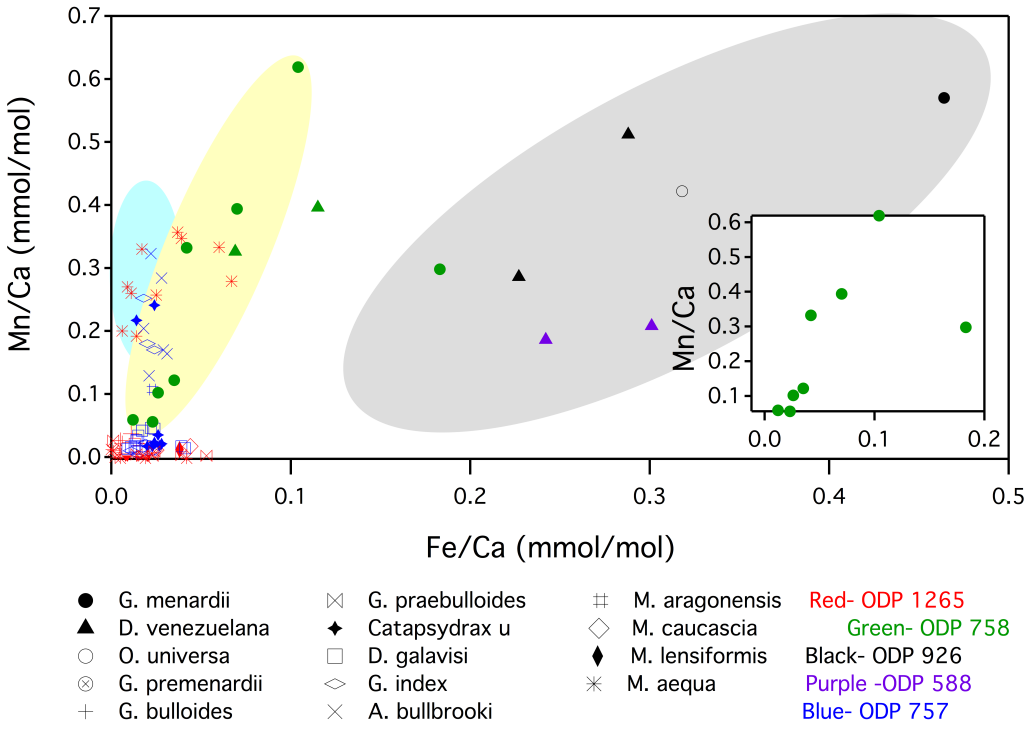

Figure S.8 - Mn/Ca against Fe/Ca for all the samples that were analyzed for foraminiferal CAS $\delta^{34}S$. Samples with high Mn/Ca and Fe/Ca ratios are grouped by colour, with high Fe/Ca and high Mn/Ca (likely ferro-manganese crusts) in grey, and low Fe/Ca with high Mn/Ca in blue, with "intermediate" Fe/Ca ratios and high Mn/Ca ratios shown in yellow (principally the Site 758 *G. menardii* samples). *G. menardii* samples from Site 758 are shown in more detail in the inset.

An upper bound on the proportion of sulfur that is associated with the contaminant manganese-rich phase can be calculated, assuming that all the *G. menardii* have the same starting sulfate concentration (500 ppm) and foraminiferal CAS $\delta^{34}S$ (22.1‰). If all of the "extra sulfate" in *G. menardii* samples with high sulfate concentrations (i.e. > 500 ppm), is from a manganese rich phase, then, comparing the number of moles of manganese and sulfate in these samples requires that this phase has a Mn/SO_4 ratio of ~2. Moreover, a mixing calculation suggests that the contaminating sulfur would have a $\delta^{34}S$ of ~24 - 26‰. This Mn/SO_4 ratio is highly unlikely in a contaminant phase: manganese-sulfate salts are very soluble, and would likely be removed easily during cleaning. The assumptions in this simple calculation are likely overestimates,

however, as the concentration of sulfate in *G. menardii* is likely to vary naturally across this time interval, and not all the "extra sulfate" is necessarily associated with a contaminant.

In spite of the potential contamination problems with *G. menardii*, the 2‰ decrease in foraminiferal CAS $\delta^{34}S$ over the past 10 Ma is still apparent, because samples from Site 926 are 2‰ elevated above modern seawater at 10 Ma, from both *G. menardii* and *D. venezuelana* (and we can constrain the sulfur isotope offset between seawater and foraminiferal CAS $\delta^{34}S$ for *G. menardii* from core-top samples). Samples in Site 926 do not show any relationship between the concentrations of trace elements in the calcite and foraminiferal CAS $\delta^{34}S$ as described for Site 758. Moreover, attempting to adjust the 10 - 0 Ma samples at Site 758 to account for potential contamination would actually reinforce the decrease in foraminiferal CAS $\delta^{34}S$ over the most recent 10 Ma, not reduce it. This is because the positive correlation between manganese and foraminiferal CAS $\delta^{34}S$ at Site 758 means that, if there was a contamination, the measured CAS $\delta^{34}S$ is, if anything higher than it should be. Therefore, correcting the data would make the foraminiferal CAS $\delta^{34}S$ even lower.

5. Carbon isotope comparison

We measured carbonate carbon isotopes in mixed benthic foraminiferal tests that were stratigraphically tied to $\delta^{34}S$ samples from our record. A comparison to the global compilation [20], indicates that the stratigraphy for these Sites can be robustly compared with the long term trends in the Zachos compilation[20] (see Figure 1).

The cross plot of carbon and sulfur isotopes was constructed using a box-car average of the $\delta^{13}C$ data, using box sizes determined by the age difference between each $\delta^{34}S$

data point from the Paleocene – Early Eocene portion of our Cenozoic curve (see Figure S.9). Our data for the Paleogene is sparse, and different foraminiferal species CAS records are not spliced together due to insufficient species overlap. Thus, to provide an estimate for the Paleogene cross-plot data, we included barite data[21,22] for the notable gaps in our data set, applying a +1‰ offset in the data, to account for the difference observed between the two records (see Figure S.10).

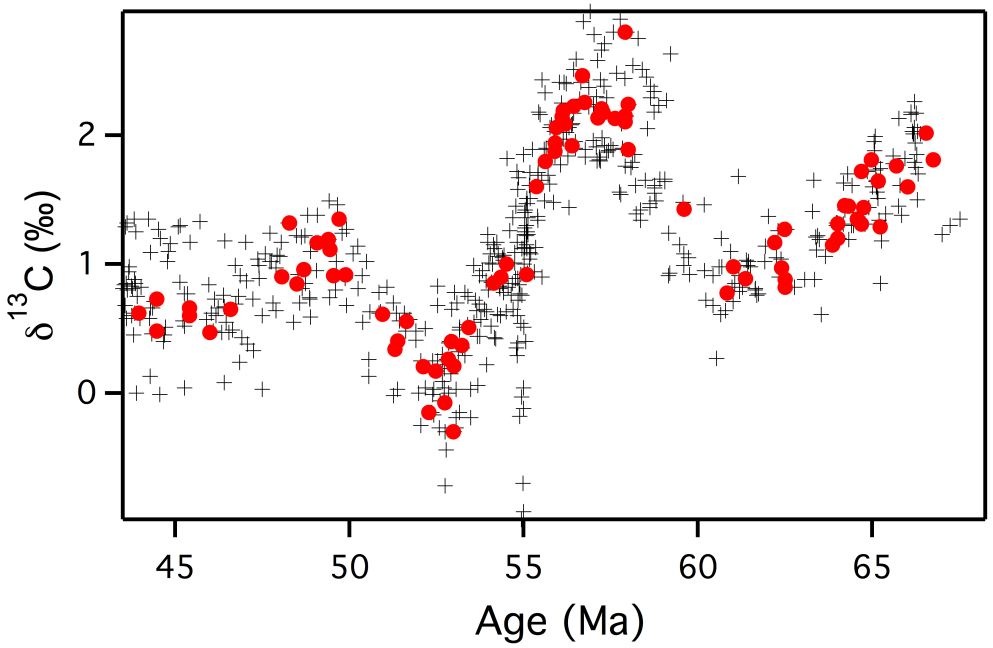

Figure S.9 - $\delta^{13}C$ from Zachos [20] (black crosses), with values of $\delta^{13}C$ calculated from the box-car averages (red circles) used in the cross plot (Figure 2).

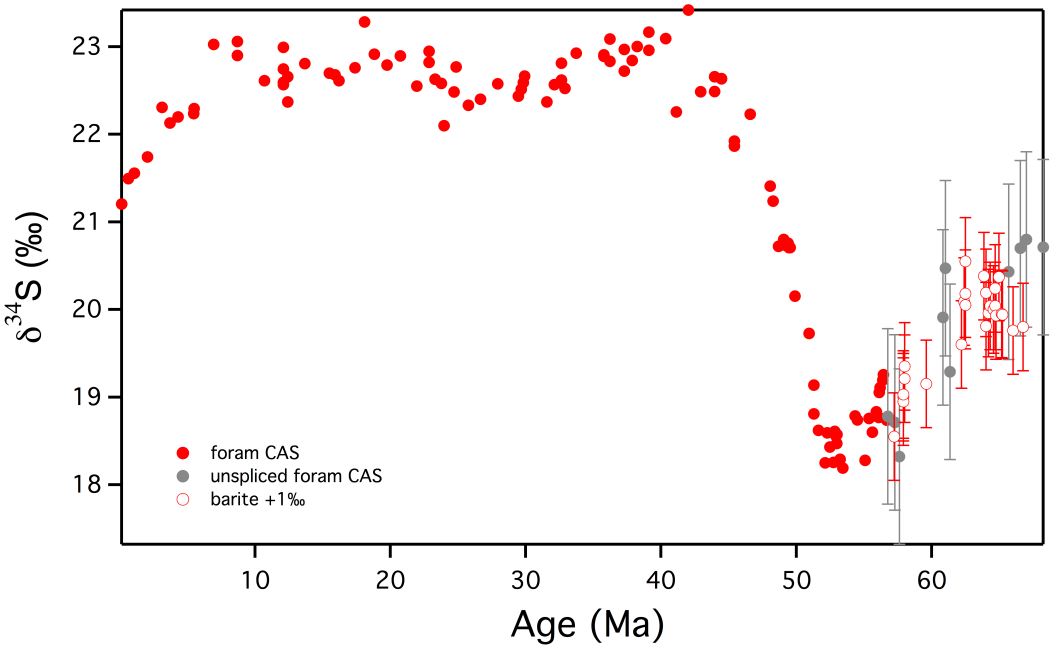

Figure S.10 – Sulfur isotope data used in the cross-plot, comprising our species-spliced data (closed red circles), non species-spliced data (grey closed circles, with error bars of ±1‰ to represent variations in $\delta^{34}S$ between species) and barite data[21] +1‰ (open red circles) where gaps in our data occur.

6. Model details

6.1 Governing equations

Changes in the concentration and isotopic composition of a chemical constituent in the ocean over time can be modeled using two mass balance relationships. The time dependent change in X, the number of moles of a given element in a reservoir can be expressed by the following equation:

$$\frac{dX}{dt} = F_{in} - F_{out} \qquad (S.1)$$

Where F_{in} is the total input flux to the ocean, and F_{out} is the sum of the fluxes that remove the element from the ocean.

The isotopic composition of the ocean can then be expressed in delta notation using the ratio of the molar concentrations of two isotopes, ^{a}X and ^{b}X, relative to a standard:

$$\delta = \left(\frac{{}^{a}X/{}^{b}X}{({}^{a}X/{}^{b}X)_{standard}} - 1\right) \times 1000 \quad \text{(S.2)}$$

Carbon isotopes

The carbon-12 specific version of equation S.1 is:

$$\frac{\partial {}^{12}C}{\partial t} = F_{W\,{}^{12}C} - F_{B{}^{12}C} \quad \text{(S.3a)}$$

Where ^{12}C is the number of moles of carbon-12 in the ocean, $F_{W\,{}^{12}C}$ is the weathering input flux of carbon-12, and $F_{B{}^{12}C}$ is the burial flux of carbon-12. The burial flux of carbon-12 can be further partitioned into the organic carbon burial flux and a carbonate burial flux $\left(F_{org{}^{12}C} + F_{carb{}^{12}C}\right)$. If we further assume a constant oceanic volume V_{Ocean},

$$V_{Ocean} \times \frac{\partial [{}^{12}C]}{\partial t} = F_{W\,{}^{12}C} - F_{B{}^{12}C} \quad \text{(S.3b)}$$

Where $[^{12}C]$ is the molar concentration of carbon-12 in the ocean. The carbonate burial flux is assumed to be a function of the concentration of DIC in the ocean ($k_{CaCO_3} \times [DIC] \times V_{Ocean}$). When multiplied by $[^{12}C]/[DIC]$ to obtain the flux of carbon-12, this becomes ($k_{CaCO_3} \times [^{12}C] \times V_{Ocean}$).

While changes in the volume of the ocean will not affect the calculated carbon sulfur

isotope ratios, a decrease in ocean volume over the Cenozoic due to continental ice growth will result in increased concentrations of DIC and sulfate in the ocean, and as a consequence, our calculated concentrations represent a lower estimate on seawater sulfate and DIC concentrations.

Substituting these terms into equation S.3b yields:

$$V_{Ocean} \times \frac{\partial[^{12}C]}{\partial t} = F_{W\,^{12}C} - F_{org^{12}C} - (k_{CaCO_3} \times [^{12}C] \times V_{Ocean}) \quad \text{(S.4)}$$

A similar equation can be written for carbon-13, if S.3 is replaced with

$$V_{Ocean} \times \frac{\partial[^{13}C]}{\partial t} = F_{W\,^{13}C} - F_{org^{13}C} - (k_{CaCO_3} \times [^{13}C] \times V_{Ocean}) \quad \text{(S.5)}$$

Equation S.5 can be written in terms of carbon-12 fluxes by multiplying each flux term by $[^{13}C]/[^{12}C]$. This is the isotopic ratio of carbon which is connected to the traditional δ^{13}C notation according to S.6:

$$\frac{[^{13}C]}{[^{12}C]} = \left(\frac{\delta^{13}C}{1000} + 1\right) \times R_C \quad \text{(S.6)}$$

Where R_C is the absolute ^{13}C/^{12}C ratio of the V-PDB international standard material. The resulting equation is:

$$V_{Ocean} \times \frac{\partial[^{13}C_{ocean}]}{\partial t} = F_{W\,^{12}C} \times {}^{12}R_{in} - F_{org^{12}C}\left(\frac{\delta^{13}C_{ocean}+\varepsilon_{org}}{1000}+1\right)\times R_C -$$

$$(k_{CaCO_3}\times[^{12}C_{ocean}]\times V_{Ocean}) \times {}^{12}R_{ocean} \qquad \text{(S.7)}$$

Where $^{12}R_{in}$ is the isotope ratio of the input, $\delta^{13}C_{ocean}$ is the isotope composition of DIC and $^{12}R_{ocean}$ its carbon isotopic ratio, and ε_{org} (defined as $\delta^{13}C_{org} = \delta^{13}C_{ocean} + \varepsilon_{org}$) is the average isotope fractionation between seawater and organic carbon reaching the seafloor.

It must be noted that this is a long-term carbon cycle model, which treats dissolved inorganic carbon in the ocean as a whole, and does not distinguish between carbonate, bicarbonate and dissolved CO_2, which will exchange on much shorter timescales within the ocean.

A similar approach can be undertaken for the sulfur cycle, such that:

$$V_{Ocean} \times \frac{\partial[^{32}S]}{\partial t} = F_{W\,^{32}S} - F_{B^{32}S} \qquad \text{(S.8)}$$

Where $[^{32}S]$ is the molar concentration of sulfur-32 in the ocean, $F_{W^{32}S}$ is the weathering input flux of sulfur-32, and $F_{B^{32}S}$ is the burial flux of sulfur-32. The burial flux of sulfur-32 can be further partitioned into a reduced sulfur burial flux (pyrite and organosulfides) and an evaporite burial flux $\left(F_{red^{32}S} + F_{evap^{32}S}\right)$.

As a first pass, the evaporite burial flux is assumed to be constant, the value of which is poised such that the sulfur cycle starts in steady state. An evaporite burial flux that

is independent of sulfate concentration is not unreasonable, as evaporite burial is likely a function more of paleogeography than of sulfate concentration [23].

Each modelling scenario was, however, re-run using an evaporite burial flux that was a function of concentration, in order to compare differences in the model output (see section 6.3.4).

Expanding the burial flux term in Equation S.8 (and recalculated in terms of sulfur-32) yields:

$$V_{Ocean} \times \frac{\partial[^{32}S]}{\partial t} = F_{W\,^{32}S} - F_{red^{32}S} - F_{evap^{32}} \quad \text{(S.9)}$$

A similar equation can be written for sulfur-34, in terms of the fluxes of sulfur-32

$$V_{Ocean} \times \frac{\partial[^{34}S]}{\partial t} = F_{W\,^{32}S} \times {}^{34}R_{in} - F_{red^{32}S}\left(\frac{\delta^{34}S_{ocean}+\varepsilon_{SO4-FeS2}}{1000}+1\right)\times {}^{34}R_s - F_{evap^{32}} \times {}^{34}R_{ocean} \quad \text{(S.10)}$$

Where $^{34}R_{in}$ is the isotope ratio of the input, $\delta^{34}S_{ocean}$ is the isotope composition of marine sulfate and $^{34}R_{ocean}$ its isotopic ratio, and $\varepsilon_{SO4-FeS2}$ (defined as $\delta^{34}S_{pyrite} = \delta^{34}S_{ocean} + \varepsilon_{SO4-FeS2}$) is the average isotope fractionation between seawater sulfate and the reduced sedimentary sulfides (namely, pyrite and organic sulfur). $^{34}R_S$ is the absolute $^{34}S/^{32}S$ ratio of the international standard material (in this case, VCDT[24]).

6.2 Input parameters

6.2.1 Carbon

6.2.1a Carbon Input flux ($F_{W\,^{12}C}$):

The standing mass of oceanic carbon, its residence time, and its input flux in the Paleogene are not well known. In the modern ocean, the mass of carbon is estimated to be 2.8x10^{18} moles, with a residence time of 100 ka[25], assuming an input of ~ 1.7x10^{13} mol/yr. For this model, we assume an input flux of carbon-12 of 2 × 10^{13} mol/yr, and a standing mass of 30,000 Pg (2.5 x 10^{18} moles, c.f.[26]).

The isotope composition of CO_2 emitted to the ocean-atmosphere system is assumed to be set by volcanism and the weathering of carbonates and silicates, and is assumed in this model to have a $\delta^{13}C$ value of -2.5‰. Therefore the input flux of carbon-13 ($(F_{W\,^{13}C}$) is taken to be $F_{W\,^{12}C}\left(\frac{\delta^{13}C_{in}}{1000}+1\right)\times R_C$ (c.f. Eqn S.7).

6.2.1b Carbon burial fluxes

Organic carbon burial flux ($F_{org^{12}C}$): The fraction of organic carbon buried is calculated by assuming that its burial sets the isotope composition of the remaining ocean. This is based upon the assumptions that: 1) the isotopic composition of the input flux to the ocean is set by the average composition of volcanism and weathering of carbonates and silicates[27]; 2) the remaining output flux (carbonate burial) has negligible fractionation from seawater[28]; and 3) the carbon isotope fractionation between seawater and organic matter is constant through time. This final assumption is an oversimplification, as the carbon isotope fractionation between DIC and organic carbon likely was larger in the Paleogene[29]. For simplicity, however, the carbon isotope fractionation is assumed to be 27‰[30] for the entirety of the Cenozoic, although this may lead to underestimates in the fractional burial of organic carbon in

the later Cenozoic. As our focus in this paper is on carbon cycling in the Paleogene and Eocene, where the variability in the carbon isotope fractionation during photosynthesis is thought to be ~1‰, which leads to a maximum uncertainty of 4%, which is small relative to the uncertainty in estimating the input flux and DIC concentration over the Paleogene.

We estimate the average $\delta^{13}C$ of DIC from a smoothed record of the Zachos data[20] (see Figure S.10) of globally distributed benthic foraminifera (corrected to *Cibiceoides*) and assume an isotopic offset of +1‰ from seawater[31]. The $\delta^{13}C$ of foraminifera depends on several factors including organic matter availability and $\delta^{13}C$ of DIC (which is not constant in each ocean basin). Nevertheless, using an average value for a global distribution of ocean basins, the long-term $\delta^{13}C$ of DIC can be estimated. This estimate directly affects the fraction of organic carbon buried, and thus the pyrite burial flux. The Zachos data was smoothed from 46–66.5 Ma, using a smoothing spline in Igor Pro v.6[32]. Prior to 46 Ma a value of 0.57‰ was used for $\delta^{13}C$. We further assume that the carbon cycle is in steady state at each time point, and that there is a linear change in organic carbon burial between each solution.

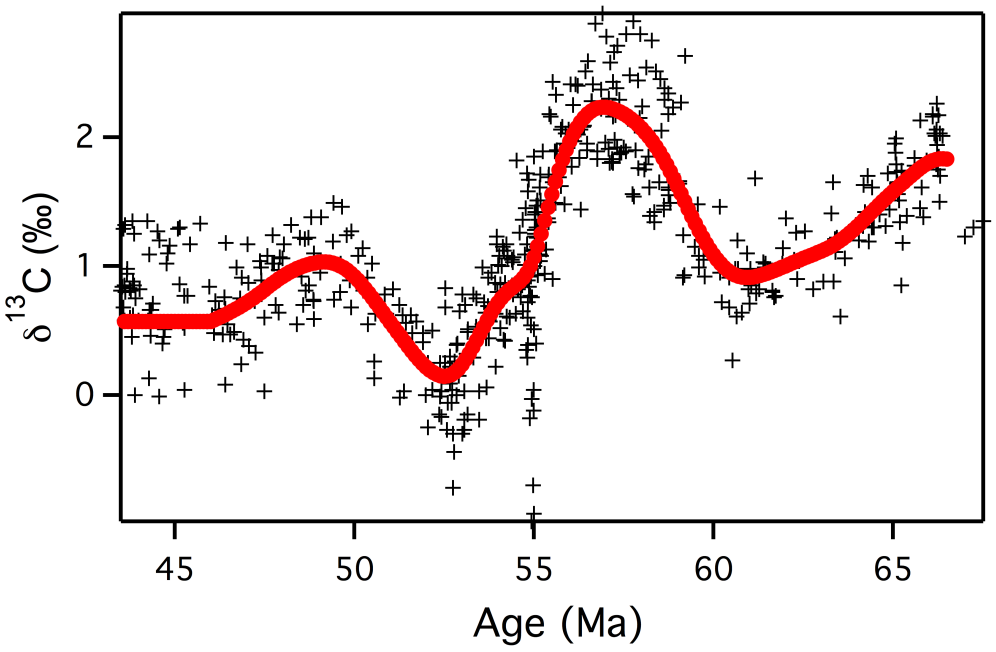

Figure S.10 – Smoothed record of foraminiferal $\delta^{13}C$ (red circles) calculated from Zachos data[20] (black crosses) using a smoothing spline in Igor Pro v.6.

Carbonate burial flux ($F_{carb^{12}C}$): we assume that the carbonate burial flux is a function of the total inorganic carbon concentration of the ocean (the sum of all the ^{12}C and ^{13}C in the ocean at any model time point), with the same carbon isotopic composition. It is tuned such that it is initially in steady state, set by F_{org}, the fractionation between organic carbon and the dissolved inorganic carbon in the ocean, and the ratio of $^{13}C/^{12}C$ in the ocean.

6.2.2 Sulfur parameters

6.2.2a Sulfate input flux ($F_{W\,^{32}S}$):

The modern day riverine flux of sulfate to the ocean is estimated to be ~1.5 to 3.5 × 10^{12} mol/yr[11,33]. The sulfur isotope composition of this riverine flux is thought to be

between 0 and 15‰ (reflecting a balance between pyrite and evaporite weathering[21,33-35]).

For the purposes of this model we assume that the only input flux of sulfate to the ocean is rivers, and is 3.5×10^{12} mol/yr. Although volcanic SO_2 is a direct source of sulfate to the ocean, this flux is small compared to the other fluxes ~$3x10^{11}$ mol/yr[36], and is unlikely to be important in the 5‰ increase in $\delta^{34}S$, which occurs over ~5 Ma. We have assumed that the $\delta^{34}S$ input to the ocean incorporates a component of this volcanic flux, and have assumed for simplicity that it is constant.

The assumption that the input flux is constant over the remainder of the Cenozoic is an over-simplification, because as sea-level falls, shallow burial environments are exposed. The exposure and weathering of epicratonic and shallow shelf environments will indeed provide a new source of both pyrite and evaporite rocks for weathering into the ocean. If, as we assume, the buried pyrite is generally isotopically heavy in these environments, then this additional input flux would predominantly affect the sulfate concentration (and may, perhaps contribute to the explanation of large sulfate concentration increases over the Cenozoic[37]), but would not significantly change the isotopic value of the input[35].

Over the remainder of the Cenozoic, as sea-level falls and shallow shelves, as sea-level and

The flux of sulfate out of the marine sulfur reservoir due to interactions with the crust (broadly termed “hydrothermal fluxes”) is not well constrained, although it is thought to be small compared to either the riverine flux of sulfate into the ocean, or the flux of

sulfur out of the ocean as evaporites and pyrite[38] (~1-2%). Consequently, the hydrothermal flux of sulfate is often deemed negligible compared to the remaining fluxes (e.g. [23]), and will not be considered further.

For the final model, the $\delta^{34}S$ value of the input flux is assumed to be 4‰, which is within the range of sulfate isotopic compositions estimated for modern global input by rivers[39].

6.2.2b Sulfur burial fluxes

Reduced sulfur burial flux ($F_{red^{32}S}$): Global sulfate reduction rates have been estimated at 8 – 11 × 10^{12} mol/yr[40,41]. A significant portion (~75 - 90%) of the reduced product (hydrogen sulfide) is re-oxidized by reaction with dissolved oxygen (or by oxidation with other chemical species - e.g. NO_3, Mn(IV) or Fe(III)) in the overlying pore fluid[42-44]). HS^- that is not re-oxidized can be removed from the system by reaction with Fe(II) to form FeS and ultimately FeS_2 (pyrite). The amount of sulfur that is removed from the marine sulfur cycle by pyrite burial has been greatly debated, with estimates ranging from 10% - 20% of the total flux out[45]; 10% to 40%[46]; to 70% – 90%[23]. In our model the reduced sulfur burial flux is assumed to be tied to the carbon burial flux by a C:S weight ratio of 1 to 3 which corresponds to a pyrite burial flux that is 20–60% of the input flux depending on the C:S ratio and the starting steady state.

Evaporite burial flux ($F_{evap^{32}S}$): evaporite formation commonly occurs in restricted marginal marine settings and sulfate evaporite precipitation (mostly gypsum and anhydrite) has a very small sulfur isotope fractionation relative to that associated with

sedimentary sulfide burial (~1.7‰,[47,48]). Evaporites are therefore isotopically close to contemporaneous seawater, except where extensive bacterial sulfate reduction in restricted marginal settings results in the distillation of ^{34}S in the sulfate pool and the resulting evaporite. It is assumed in the model that these restricted marginal settings represent closed systems, where seawater sulfate is effectively separated from the ocean and stored as evaporites, and thus any fractionation prior to deposition does not affect seawater sulfate as a whole (i.e., there is no return flux of sulfate back to the ocean from these environments).

Sulfate precipitation from seawater is highly episodic, and so evaporite fluxes can vary dramatically, from minimal precipitation today, to large-scale evaporite deposits in the Devonian and Permian[49]. One suggestion has been that evaporite formation does not scale with marine sulfate concentration[23]. Instead it is dependent on the availability of suitable environments for the formation and preservation of evaporites, and therefore on local basinal tectonics. It is thus likely to be highly variable over time. The estimated burial rate for "long-term" evaporites over the Phanerozoic (rather than evaporites which are a part of the "net flux" of evaporite deposition and weathering) is estimated to be 3.3 - 4.5 × 10^{11} molS/yr on average[23].

6.3 Model experiments and results

The data was divided into two temporal phases. Phase 1 (66.5-52.6 Ma) encompasses the 1.5‰ decrease in $\delta^{34}S$, during which time the $\delta^{13}C$ decreases to 1‰, increases to 2‰, and then finally decreases to 0‰. Phase 2 (52.6 Ma onwards) comprises the 5‰ increase in $\delta^{34}S$ and the 1‰ increase, and subsequent 0.5‰ decrease in $\delta^{13}C$.

Three different sets of parametrization of the pyrite burial model input were used in the model. First (section 6.3.1), the impact of pyrite burial alone was considered on the sulfur cycle, assuming the carbon and sulfur cycles are tightly coupled via organic carbon burial. Second, (section 6.3.2) pyrite burial flux was split into two fluxes with differing sulfur isotope fractionations between sulfate and pyrite ($^{34}\varepsilon_{SO4\text{-}pyr}$): a "nearshore" ($^{34}\varepsilon_{SO4\_pyr\_nearshore}$ pyrite with a relatively small fractionation from seawater sulfate) and an "open ocean" outflux ($^{34}\varepsilon_{SO4\_pyr\_deep}$ with a much larger fractionation). Third, in the last version of the model (section 6.3.3), the pyrite burial flux was partially decoupled from the organic carbon flux for the period prior to 52.6 Ma. It was assumed that only part of the $\delta^{13}C$ record was due to organic carbon burial in environments where pyrite burial was coupled, with the remaining $\delta^{13}C$ change being due to terrestrial carbon burial, methane and volcanic fluxes. A burial flux for pyrite was assumed, which decreased slowly to 52.6 Ma, roughly tracing the long-term decrease in $\delta^{13}C$, over which the larger carbon isotope fluctuations are superimposed.

Section 6.3.4 then explores the result of changing the evaporite burial flux from a constant to a concentration dependent term ($k_{evap} \times [SO_4] \times V_{ocean}$) for all the previous modelling scenarios, in order that sulfate concentrations return to steady state. Another means of reaching steady state, by altering the C:S burial ratio at 52.6 Ma, such that pyrite burial returns to similar levels as in the Paleocene, is shown for model scenarios involving a change in $^{34}\varepsilon_{SO4\text{-}pyr}$ (i.e., model scenarios in 6.3.2 and 6.3.3).

We then demonstrate (in sections 6.3.5 - 6.3.7) that these solutions are not unique, by showing similar outputs for our model that better replicate the data (i.e., section 6.3.3)

using different model inputs (sulfate input fluxes and sulfate concentrations), pyrite burial fluxes (C:S ratios) and a wider range of sulfate-pyrite isotope fractionations.

Finally, in section 6.3.8, we test the model sensitivity to the assumption that pyrite burial is limited by the supply of reactive iron, and thus when pyrite burial is supressed in shallow environments, pyrite burial correspondingly increases in deeper environments. We show that the observed 5‰ increase in $\delta^{34}S$ can still be replicated by the model using the range of parameters for the sulfur cycle as reported in the literature, but necessitates a slightly larger change in ${}^{34}\varepsilon_{SO4\text{-}pyr}$.

Section and figure	Model description[a]	$[SO_4]_{init}$ mM	F_{in} 10^{12} mol/yr	F_{evap} 10^{12} mol/yr	$^{34}\varepsilon_{SO4\text{-}pyr}$[c]	f_{marine}	C:S (wt.%)
6.3.1 (a) Fig S.11	Model starts at 52.6 Ma	2.8	3.5	Fixed at 2.08	constant and unsplit, -35.65‰		1
6.3.1 (b) Fig S.11	Model starts at 66.5 Ma	11.2	3.5	Fixed at 1.43	constant and unsplit, -27.4‰		1
6.3.2 Fig S.12	$^{34}\varepsilon_{global\_average}$ changes at 52.6 Ma	11.2	3.5	Fixed at 1.43	split $^{34}\varepsilon_{SO4\_pyr\_deep}$ = -41‰, (initial $^{34}\varepsilon_{global\_average}$ = -27.4‰)	0.64 to 1	1
6.3.3 Fig S.13	F_{pyr} only coupled to F_{org} after 52.6 Ma, $^{34}\varepsilon_{global\_average}$ changes at 52.6 Ma	11.2	3.5	Fixed at 1.4	split $^{34}\varepsilon_{SO4\_pyr\_deep}$ = -35.5‰, (initial $^{34}\varepsilon_{global\_average}$ = -27‰)	0.74 to 1, ramped over 0.5 Ma	0.86
6.3.4 (a) Fig S.14	Model starts at 52.6 Ma	11.2	3.5	variable[b] $k_{evap}=5.62\times10^{-7}$ yr^{-1}	constant and unsplit, -35.65‰		1
6.3.4 (b) Fig S.14	Model starts at 66.5 Ma	11.2	3.5	variable[b] $k_{evap}=9.68\times10^{-8}$ yr^{-1}	constant and unsplit, -27.4‰		1
6.3.4 (c) Fig S.15	F_{pyr} coupled to F_{org}, $^{34}\varepsilon_{global\_average}$ changes at 52.6 Ma	11.2	3.5	variable[b] $k_{evap}=9.68\times10^{-8}$ yr^{-1}	split $^{34}\varepsilon_{SO4\_pyr\_deep}$ = -41‰, (initial $^{34}\varepsilon_{global\_average}$ = -27.4‰)	0.64 to 1	1
6.3.4 (d) Fig S.16	F_{pyr} only coupled to F_{org} after 52.6 Ma, $^{34}\varepsilon_{global\_average}$ changes at 52.6 Ma	11.2	3.5	variable[b] $k_{evap}=9.46\times10^{-8}$ yr^{-1}	split $^{34}\varepsilon_{SO4\_pyr\_deep}$ = -35.5‰, (initial $^{34}\varepsilon_{global\_average}$ = -27‰)	0.74 to 1, ramped over 0.5 Ma	0.86
6.3.4 (e) Fig S.17	$^{34}\varepsilon_{global\_average}$ changes at 52.6 Ma C:S decreases at 52.6 Ma	11.2	3.5	Fixed at 1.43	split $^{34}\varepsilon_{SO4\_pyr\_deep}$ = -31‰, (initial $^{34}\varepsilon_{global\_average}$ = -27.4‰)	0.87 to 1	1 to 0.76
6.3.4 (f) Fig S.18	F_{pyr} only coupled to F_{org} after 52.6 Ma, $^{34}\varepsilon_{global\_average}$ changes at 52.6 Ma C:S decreases at 52.6 Ma	11.2	3.5	Fixed at 1.4	split $^{34}\varepsilon_{SO4\_pyr\_deep}$ = -35.5‰, (initial $\varepsilon_{global\_average}$ = -30.7‰)	0.85 to 1, ramped over 0.5 Ma	0.86 to 0.76
6.3.5 (a) Fig S.19	F_{pyr} only coupled to F_{org} after 52.6 Ma, $^{34}\varepsilon_{global\_average}$ changes at 52.6 Ma	5.6	1.5	Fixed at 0.6	split $^{34}\varepsilon_{SO4\_pyr\_deep}$ = -35.5‰, (initial $^{34}\varepsilon_{global\_average}$ = -27‰)	0.74 to 1, ramped over 0.5 Ma	2
6.3.5 (b) Fig S.19	F_{pyr} only coupled to F_{org} after 52.6 Ma, $^{34}\varepsilon_{global\_average}$ changes at 52.6 Ma	8.4	2.5	Fixed at 1	split $^{34}\varepsilon_{SO4\_pyr\_deep}$= -35.5‰, (initial $^{34}\varepsilon_{global\_average}$ = -27‰)	0.74 to 1, ramped over 0.5 Ma	1.2
6.3.6 (a)	F_{pyr} only coupled to F_{org} after 52.6 Ma, $^{34}\varepsilon_{global\_average}$ changes at 52.6 Ma	11.2	3.5	Fixed at 2.6	split $^{34}\varepsilon_{SO4\_pyr\_deep}$= -82‰, (initial $^{34}\varepsilon_{global\_average}$ = -62.8‰)	0.75 to 1, ramped over 0.5 Ma	2

6.3.6 (b)	F_{pyr} only coupled to F_{org} after 52.6 Ma, $^{34}\varepsilon_{global\_average}$ changes at 52.6 Ma Carbon fluxes all doubled	11.2	2.5	Fixed at 1.7	split $^{34}\varepsilon_{SO4\_pyr\_deep}$= -41.2‰, (initial $^{34}\varepsilon_{global\_average}$ = -31.4‰)	0.74 to 1, ramped over 0.5 Ma	1.2
6.3.7 (a) Fig 2, S.20	F_{pyr} only coupled to F_{org} after 52.6 Ma, $^{34}\varepsilon_{global\_average}$ changes at 52.6 Ma	11.2	3.5	Fixed at 1.7	split $^{34}\varepsilon_{SO4\_pyr\_deep}$= -35.5‰, $^{34}\varepsilon_{SO4\_pyr\_nearshore}$= -20‰, (initial $^{34}\varepsilon_{global\_average}$ = -27‰)	0.69 to 1, ramped over 0.5 Ma	1
6.3.7 (b) Fig 2, S.20	F_{pyr} only coupled to F_{org} after 52.6 Ma, $^{34}\varepsilon_{global\_average}$ changes at 52.6 Ma	11.2	3.5	Fixed at 1.4	split $^{34}\varepsilon_{SO4\_pyr\_deep}$= -41.2‰, $^{34}\varepsilon_{SO4\_pyr\_nearshore}$= -20‰, (initial $^{34}\varepsilon_{global\_average}$ = -27.4‰)	0.55 to 1, ramped over 0.5 Ma	1
6.3.7 (c) sensitivity range. See table S.3	F_{pyr} only coupled to F_{org} after 52.6 Ma, $^{34}\varepsilon_{global\_average}$ changes at 52.6 Ma	11.2	3.5	Fixed at 1.7	split $^{34}\varepsilon_{SO4\_pyr\_deep}$= -33‰ to -60‰, $^{34}\varepsilon_{SO4\_pyr\_nearshore}$= -3‰ to -20‰, (initial $^{34}\varepsilon_{global\_average}$ = -25.1‰ to -47.1‰)	Initially varies between 0.75 and 0.6 to 1, ramped over 0.5 Ma	0.8 to 1.5
6.3.8	F_{pyr} only coupled to F_{org} after 52.6 Ma, $^{34}\varepsilon_{global\_average}$ changes at 52.6 Ma F_{pyr_deep} doesn't increase at 52.6 Ma, ($F_{\_pyr\_deep}$=$F_{\_pyr\_total}$*$f_{marine\_initial}$ throughout)	11.2	3.5	Fixed at 1.4	split $^{34}\varepsilon_{SO4\_pyr\_deep}$= -47.9‰, (initial $^{34}\varepsilon_{global\_average}$ = -27.4‰)	0.74 to 1, ramped over 0.5 Ma	0.86

[a]except when stated otherwise, C:S is constant and equals 1 the models starts at 66 Ma, F_{pyr} coupled to F_{org} from 66.5 Ma ; [b]: variable evaporite burial is $k_{evap}\times[SO_4]\times Vol_{Ocean}$; [c]: when $^{34}\varepsilon$ is split between deep ocean and nearshore, $^{34}\varepsilon_{nearshore\ pyr}$ = -3‰, unless otherwise stated.

Table S.2. Model details and parameters

6.3.1 Pyrite burial coupled to carbon burial

The model was run (a) from 52.6 Ma and (b) for the entirety of the Paleogene. The model results demonstrate that pyrite burial coupled to organic carbon burial alone cannot adequately explain the 5‰ increase in $\delta^{34}S$, and predicts too much structure in the $\delta^{34}S$ record due to the oscillating $\delta^{13}C$ values.

a) Starting at 52.6 Ma

The model was started in steady state (with respect to sulfur and carbon concentrations and isotope ratios in the ocean) at 52.6 Ma, with an initial $\delta^{34}S$ and $\delta^{13}C$ of the ocean of 18.5‰ and 0.1‰, respectively. Input values for the model (listed in Table 2) were chosen such that it started in steady state. Model results replicate an increase in $\delta^{34}S$ and $\delta^{13}C$, with two main limitations. For sulfate concentrations > 2.8 mM (at an input flux of 3.5×10^{12} mol/yr), the increase in $\delta^{34}S$ is too slow relative to the increase in $\delta^{13}C$ (see Figure S.11). Furthermore the final steady state $\delta^{34}S$ is only 2‰ higher than the initial steady state, due to the decrease in $\delta^{13}C$ from 49.5 Ma, suggesting that pyrite burial can only account for roughly half of the increase in $\delta^{34}S$ (see Figure S.11). Moreover, when running this model using a starting sulfate concentration of 2.8 mM, and a continued increase in pyrite burial to maintain the new high $\delta^{34}S$, all sulfate is buried within 20 million years and the ocean runs out of sulfate at 32 Ma.

b) starting at 66.5 Ma

The model was started at 66.5 Ma with initial sulfate $\delta^{34}S$ and DIC $\delta^{13}C$ values of 20.2‰ and 1.8‰, respectively. Input values for the model (Table 2) were chosen such that it was initially in steady state. The model results fail to replicate either the long-

term decrease in $\delta^{34}S$, or the increase in $\delta^{34}S$ after 52.6 Ma (see Figure S.11). The long-term decrease in $\delta^{34}S$ cannot be replicated because of the coupling between organic carbon and pyrite burial: when organic carbon burial increases (and therefore so does $\delta^{13}C$ of DIC), pyrite burial and $\delta^{34}S$ must increase. Thus, the only vectors on the carbon-sulfur cross-plot can be those with both $\delta^{13}C$ and $\delta^{34}S$ increasing or decreasing. However, from 61-56.5 Ma, $\delta^{34}S$ decreases while $\delta^{13}C$ increases. The only occasions where such carbon-sulfur vectors are likely in this model are when the sulfur cycle is still returning to steady state from a previous perturbation- effectively decoupling the carbon and sulfur cycles. This only applies for very large changes in the carbon burial flux, such as the large decrease in $\delta^{13}C$ from 56.5 to 52.6 Ma. This large decrease in organic carbon and pyrite burial fluxes pushes the sulfur cycle to a new steady-state condition with a much lower $\delta^{34}S$, such that the subsequent increase in pyrite burial is not large enough to prevent the sulfur cycle ending at a new steady state with a lower seawater sulfate isotope composition than before. This result suggests that pyrite burial prior to 52.6 Ma cannot be directly coupled to organic carbon burial as modelled from the $\delta^{13}C$ of DIC.

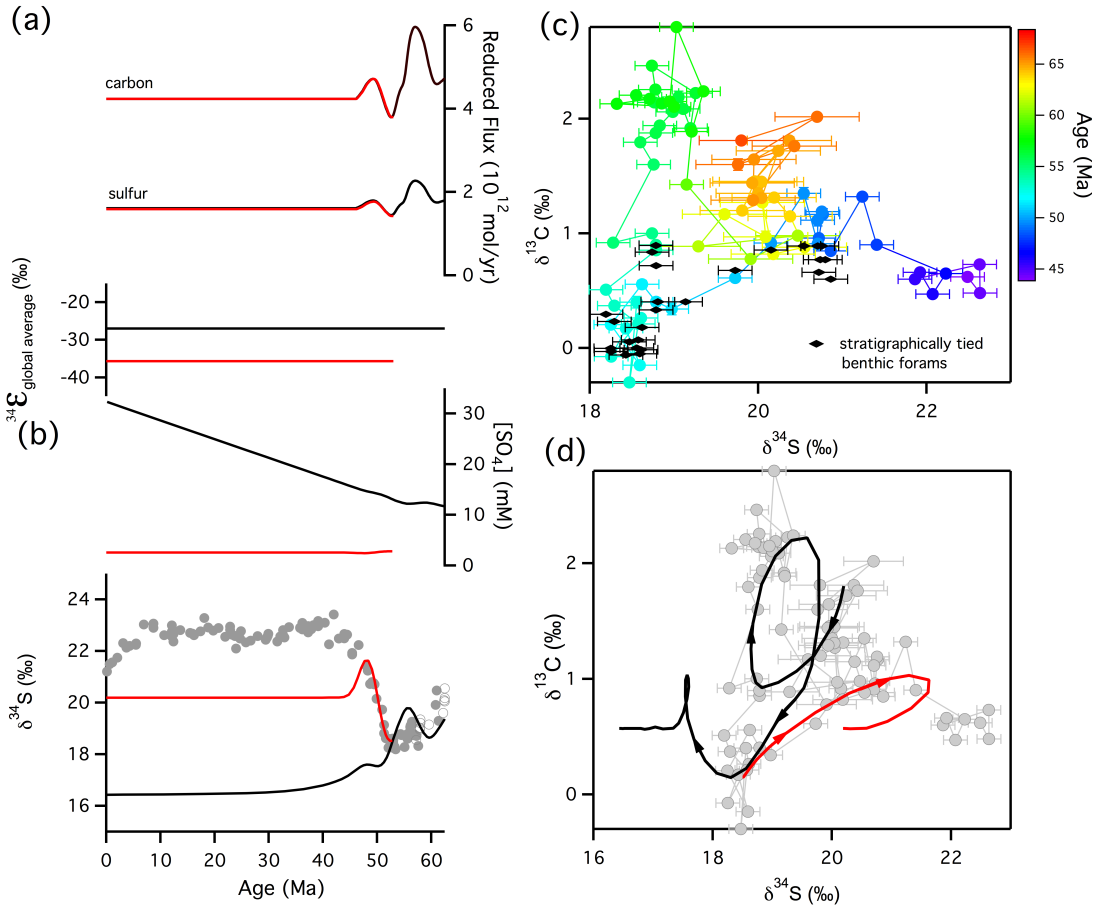

Figure S.11 – a) model input parameters and (b) $\delta^{34}S$ and sulfate concentration outputs for sulfur-carbon model runs with pyrite burial flux coupled to the organic carbon burial flux. Model runs start at 52.6 Ma (red lines) or at 66.5 Ma (black lines) c) $\delta^{13}C$ vs. $\delta^{34}S$ box-car plot with (d) model results superimposed.

6.3.2 Pyrite burial coupled to carbon burial, with a decrease in $^{34}\varepsilon_{SO4\text{-}pyr}$

The model was run from 66.5 Ma, starting in steady state (input parameters for the model were chosen such that it started in steady state, and are listed in Table 2), with initial sulfate $\delta^{34}S$ and DIC $\delta^{13}C$ values of 20.2‰ and 1.8‰, respectively. The pyrite burial flux was split into two terms, a "deep ocean" pyrite flux, and a "nearshore" epicratonic/shallow sea flux, with fractionations of $^{34}\varepsilon_{deep}$ = -41‰ and $^{34}\varepsilon_{nearshore}$ = -3‰, respectively. As a result, equation S.9 and S.10 are rewritten, resulting in a global reduced output flux characterized by an overall fractionation $^{34}\varepsilon_{global\_average}$:

$$V_{Ocean} \times \frac{\partial[^{32}S]}{\partial t} = F_{W\,^{32}S} - f_{marine} \times F_{red^{32}S} - (1 - f_{marine}) \times F_{red^{32}S} - F_{evap^{32}} \quad \text{(S.11)}$$

$$\begin{aligned} V_{Ocean} \times \frac{\partial[^{34}S]}{\partial t} &= F_{W\,^{32}S} \times {}^{34}R_{in} \\ &- f_{marine} \times F_{red^{32}S} \left(\frac{\delta^{34}S_{ocean} + \varepsilon_{deep\ pyr}}{1000} + 1 \right) \times {}^{34}R_S \\ &- (1 - f_{marine}) \times F_{red^{32}S} \left(\frac{\delta^{34}S_{ocean} + \varepsilon_{nearshore\ pyr}}{1000} + 1 \right) \\ &\times {}^{34}R_S \\ &- F_{evap^{32}} \times {}^{34}R_{ocean} \end{aligned} \quad \text{(S.12)}$$

Where f_{marine} is the ratio of deep ocean to total pyrite burial (between 0 and 1). All other symbols are the same as equations S.9 and S10.

An initial f_{marine} value of 0.64 was chosen (i.e. 64% of pyrite burial was open ocean). At 52.6 Ma, R increased to 1, so that all burial was open ocean. This decreased $^{34}\varepsilon_{global\_average}$ from -27.4‰ to -41‰. Increasing f_{marine} to 1 at 52.6 Ma implies a switch to normal open ocean pyrite burial at 52.6 Ma, as epicratonic near-quantitative and shallow shelf pyrite burial declines. This rests on the assumption that iron delivery and supply is a dominant control on sedimentary pyrite burial, rather than the supply of sulfide as in the modern ocean[50].

Model results are able to replicate the increase in $\delta^{34}S$ after 52.6 Ma using an initial sulfate concentration of 11.2 mM, however, as before, it cannot replicate the slow

decrease in $\delta^{34}S$ prior to 52.6 Ma (see Figure S.12). Sulfate concentrations do not return to steady state but gradually increase over the remainder of the Cenozoic and overestimate modern concentrations (see Figure S.12).

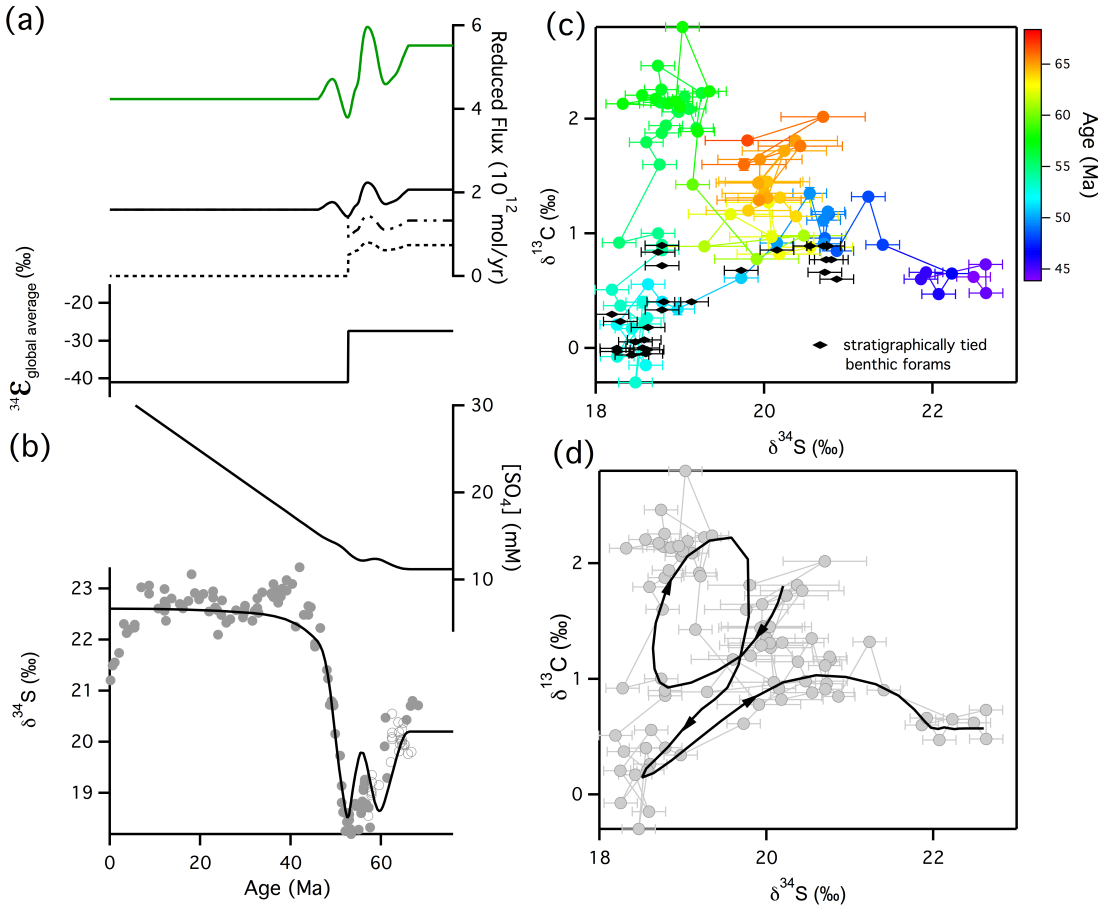

Figure S.12 – a) model input parameters and (b) $\delta^{34}S$ and sulfate concentration outputs for sulfur-carbon model runs with pyrite burial flux coupled to the organic carbon burial flux. The total pyrite burial flux (solid black line) was divided into a near-quantitative (dashed) and marine (dotted) fluxes, with large and small fractionations, respectively.). c) $\delta^{13}C$ $\delta^{34}S$ box-car plot with d) model results superimposed.

6.3.3 Pyrite burial partially decoupled from carbon prior to 52.6 Ma

The inability of the model to match phase 1 (66.5–52.6 Ma) suggests that $\delta^{13}C$ and $\delta^{34}S$ records are not fully coupled over this time period. Carbon and sulfur isotopes can be decoupled by burial in different environments[21], or by effects to the carbon

cycle that have a minimal effect on the sulfur cycle, such as volcanism or the release of carbon from methane hydrates[26]. The variability in the $\delta^{13}C$ record is likely due to more than variations in organic carbon burial over this time[26,51]. Thus, an arbitrary pyrite burial flux was assumed for the period 66.5–52.6 Ma, which roughly traced the long-term average decrease in $\delta^{13}C$ (see Figure 2a), after which the pyrite burial flux was again based an organic carbon burial flux estimated from foraminiferal $\delta^{13}C$. Input values (Table 2) were chosen such that the model started in steady state. The model results fit the data for an initial sulfate concentration of 11.2 mM. As in the previous model conditions, sulfate concentrations do not return to steady state, but increase slowly to 23 mM over the Cenozoic.

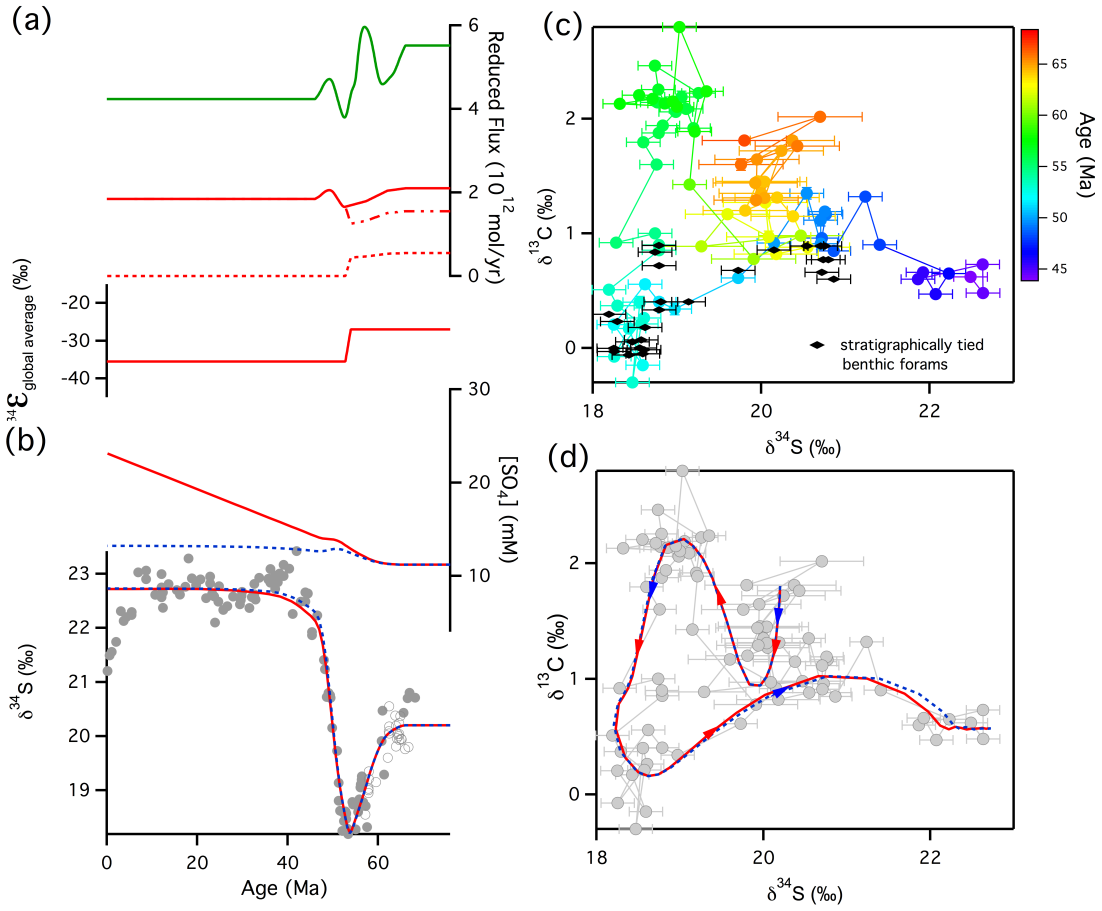

Figure S.13 – a) model input parameters and (b) $\delta^{34}S$ and sulfate concentration outputs for sulfur-carbon model runs with pyrite burial flux coupled to the organic carbon burial flux only after 52.6 Ma. Prior to 52.6 Ma the

burial flux is assumed to decrease roughly in line with the long-term overall decrease in $\delta^{13}C$. The total pyrite burial flux (solid red line) was divided into a near-quantitative (dashed) and marine (dotted) fluxes, with large and small fractionations, respectively.). c) $\delta^{13}C$ $\delta^{34}S$ box-car plot with d) model results superimposed.

This modelling result suggests that the coupling between sulfur and carbon evolved during changes in burial environments, which also shifted the locus of pyrite burial into deeper settings and increased the average fractionation between sulfate and pyrite.

6.3.4 Steady state solutions

The modelling scenarios in earlier sections have decreasing pyrite burial fluxes over the course of the model run (except for model 6.3.1a – starting at 52 Ma). Thus, with a fixed evaporite burial flux and input flux, sulfate concentrations in the ocean slowly increase over the model run. As neither pyrite nor evaporite burial are linearly dependent on sulfate concentrations[23], it is not necessarily the case that burial fluxes would increase with increasing seawater sulfate concentrations. Steady state solutions can be generated however, by replacing the constant evaporite burial with a concentration-dependent term ($k_{evap} \times [SO_4] \times V_{ocean}$). Comparisons between the model solutions from previous sections, and those with a differing evaporite burial flux (but identical in other respects) are shown in Figures S14-16.

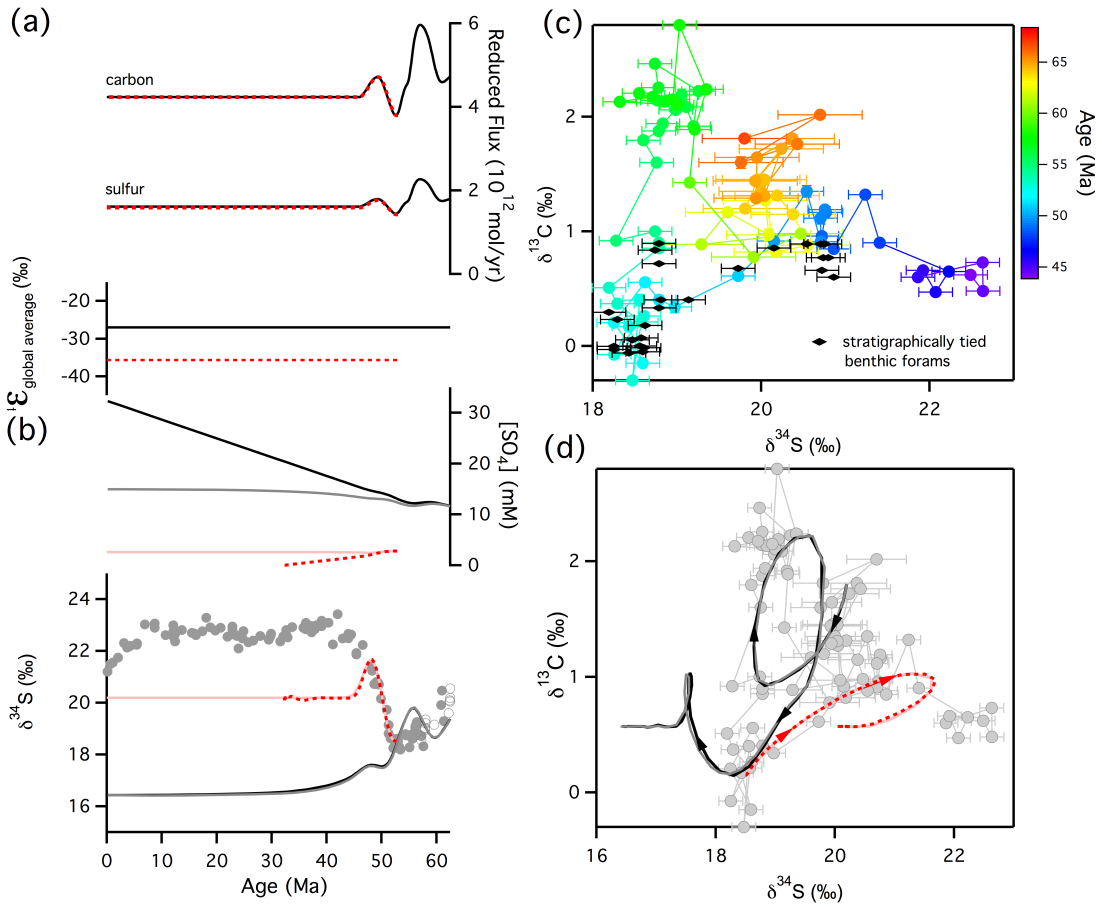

Figure S.14 – a) model input parameters (organic carbon and pyrite burial fluxes) and (b) $\delta^{34}S$ and sulfate concentration model outputs for sulfur-carbon model runs with coupled pyrite burial and organic carbon burial fluxes. Model runs starting at 52.6 Ma with either fixed (red lines) or concentration-dependent (pink lines) evaporite burial fluxes (for the same pyrite burial flux), as do model runs starting at 66.5 Ma with either fixed (black lines) or concentration-dependent (grey lines) evaporite burial fluxes . Organic carbon and pyrite burial fluxes from 66.5 Ma and from 52.6 Ma are shown as black and red lines, respectively. c) $\delta^{13}C$ $\delta^{34}S$ box-car plot with d) model results superimposed.

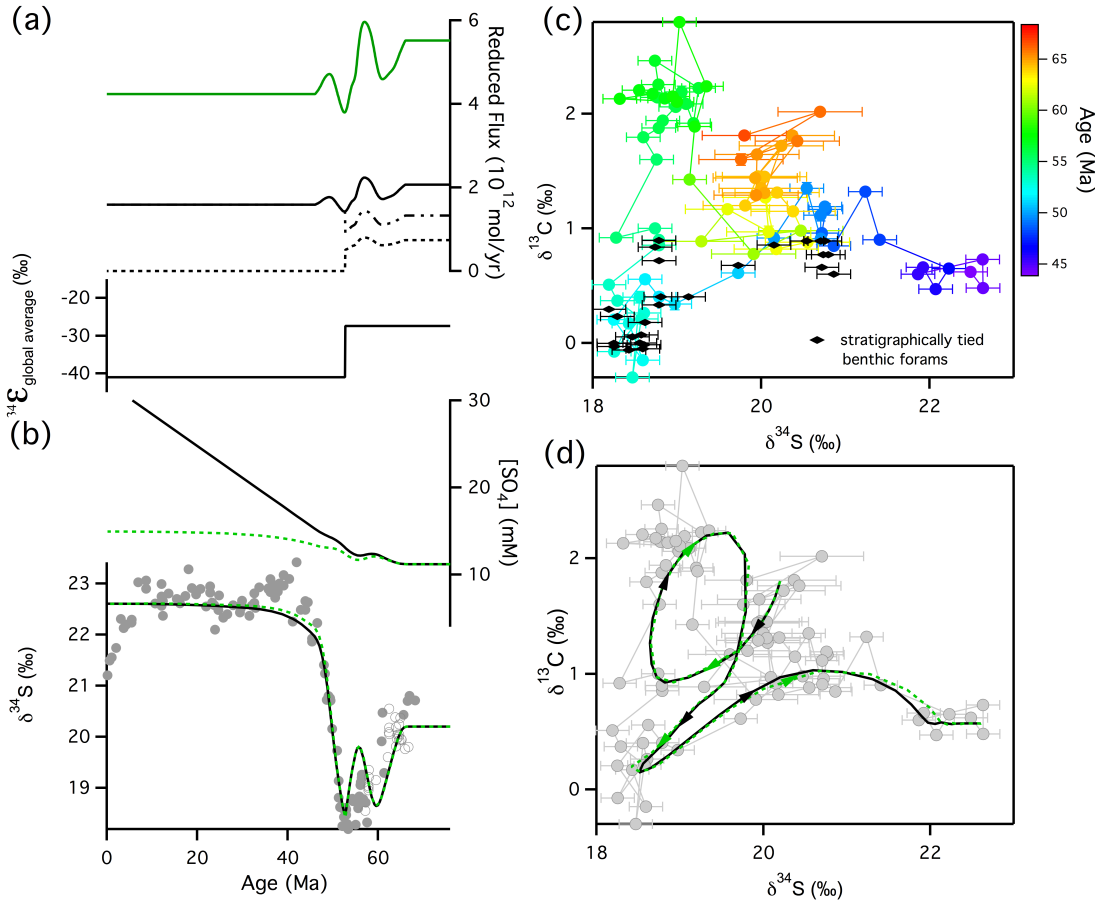

Figure S.15 – a) model input parameters and (b) $\delta^{34}S$ and sulfate concentration model outputs for sulfur-carbon model runs with the pyrite burial flux coupled to the organic carbon burial flux. Models had either fixed (black solid lines) or concentration-dependent (green dashed lines) evaporite burial fluxes for the same pyrite burial fluxes (solid black line) which was divided into a near-quantitative (dashed) and a marine (dotted) fluxe (with large and small fractionations, respectively). c) $\delta^{13}C$ $\delta^{34}S$ box-car plot with d) model results superimposed.

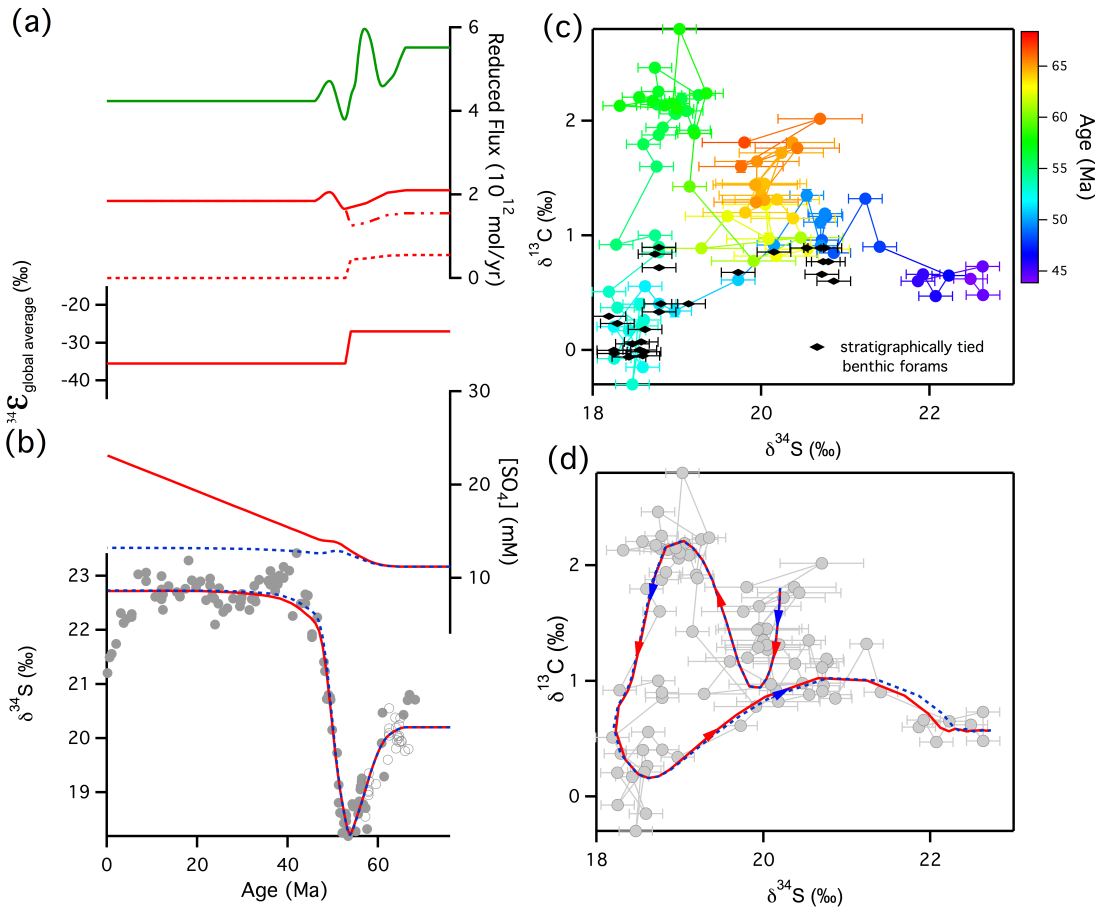

Figure S.16 – a) model input parameters and (b) $\delta^{34}S$ and sulfate concentration model outputs for two sulfur-carbon model runs with fixed (red lines) and concentration-dependent (blue dashed lines) evaporite burial fluxes. Pyrite burial fluxes were the same for both models, and were coupled to the organic carbon burial flux after 52.6 Ma. Prior to 52.6 Ma the burial flux was assumed to decrease roughly in line with the long-term overall decrease in $\delta^{13}C$. c) $\delta^{13}C$ $\delta^{34}S$ box-car plot with d) model results superimposed.

Steady state solutions can also be generated by increasing pyrite burial fluxes by changing C:S burial ratios at ~52 Ma, such that the value of the final pyrite burial flux is the same as the initial pyrite burial flux (for example, for the partially coupled case, pyrite fluxes start and end at a value of 4.8 x 10^{12} mol/yr, rather than ending at 4.2 x 10^{12} mol/yr). The change in C:S required is small (0.86 to 0.76 wt. ratio for the partially coupled model and 1 to 0.78 wt. ratio for the fully coupled model). Carbon

and sulfur isotope records suggest that the relationship between carbon and sulfur changes at 52.6 Ma, and modelling results suggest that carbon and sulfur burial environments may change, which would also lead to variations in the burial ratio between carbon and sulfur. Comparisons between model outputs for 6.3.2 and 6.3.3 with those that have varying C:S ratios is shown in Figures S.17&18.

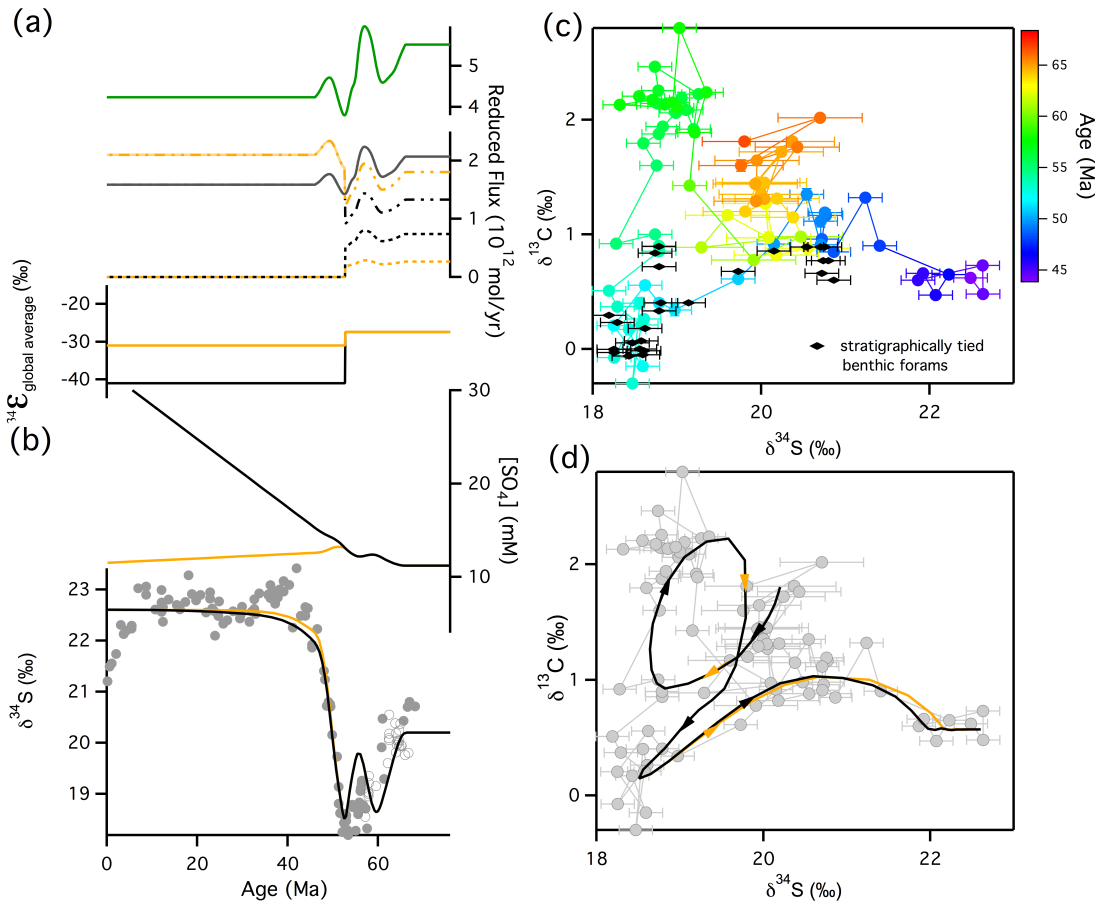

Figure S.17 – a) model input parameters and (b) $\delta^{34}S$ and sulfate concentration outputs for sulfur-carbon model runs with the pyrite burial flux coupled to the organic carbon burial flux. Models had constant C:S ratios (black lines) and a slight decrease in C:S ratio at 52.6 Ma (orange lines). The total pyrite burial flux (solid line) was divided into a near-quantitative (dashed) and marine (dotted) fluxes, with large and small fractionations, respectively.). c) $\delta^{13}C$ $\delta^{34}S$ box-car plot with d) model results superimposed.

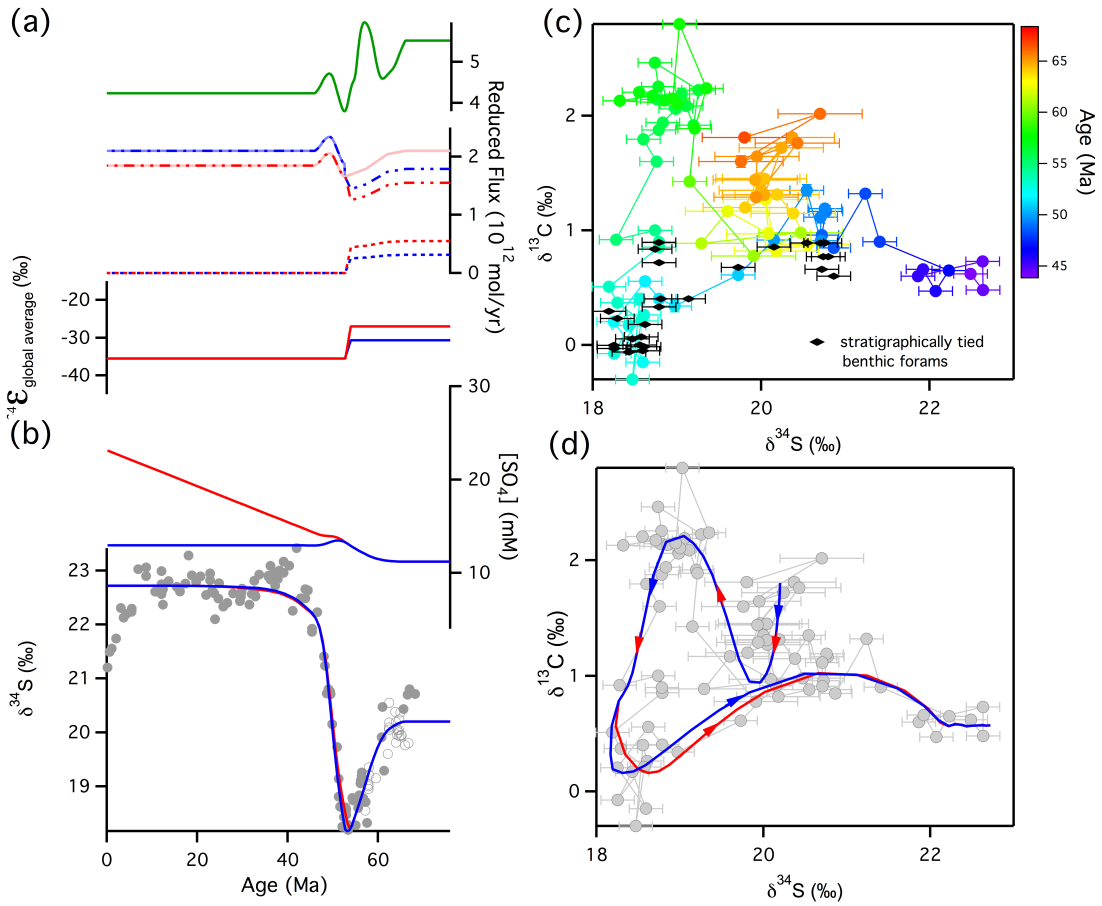

Figure S.18 – a) model input parameters and (b) $\delta^{34}S$ and sulfate concentration outputs for sulfur-carbon model runs with the pyrite burial flux coupled to the organic carbon burial flux after 52.6 Ma, with an arbitrary burial flux prior to that. Models had constant C:S ratios (red lines) and a slight decrease in C:S ratio at 52.6 Ma (blue lines). The total pyrite burial flux (solid line) was divided into a near-quantitative (dashed) and marine (dotted) fluxes, with large and small fractionations, respectively.). c) $\delta^{13}C$ $\delta^{34}S$ box-car plot with d) model results superimposed.

6.3.5 changing sulfate input flux

Using a sulfate input flux of 3.5×10^{12} mol/yr, the model fits the data best with a concentration of 11.2 mM. The key to getting the rate of $\delta^{34}S$ rise correct at 52.6 Ma is the residence time of sulfate in the ocean, a value that can change with either the

inventory of SO_4 or the input flux from rivers. There are therefore model solutions that fit the data equally well with similar residence times for sulfate, but different sulfate concentrations and input fluxes. Two examples are compared with model result from 6.3.3 in Figure S.19 (with seawater sulfate concentrations of 8.4 and 5.6 mM, and input fluxes of 2.5×10^{12} and 1.5×10^{12}, and C:S ratios of 1.2 and 2 wt.%, respectively).

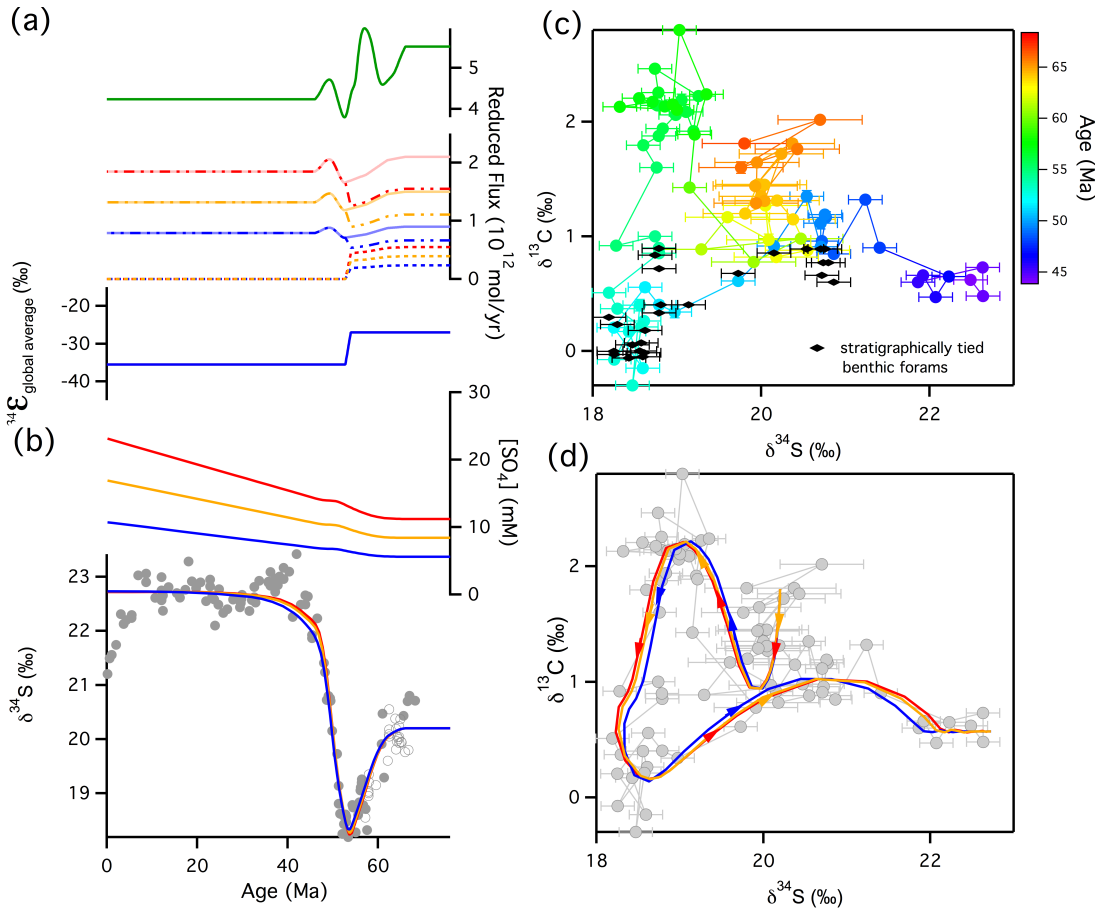

Figure S.19 –(a) model input parameters and (b) $\delta^{34}S$ and sulfate concentration outputs for sulfur-carbon model runs using an arbitrary carbon burial flux prior to 52.6 Ma. The solution as described in section 6.3.3 (red lines) compared with solutions using sulfate input fluxes of 2.5×10^{12} mol/yr (orange line) and 1.5×10^{12} mol/yr (blue line). Evaporite burial fluxes are 1×10^{12} mol/yr and 0.6×10^{12} mol/yr respectively.

6.3.6 Sensitivity to the C:S ratio and the initial conditions.

The modelling scenarios presented here so far start in steady state with an organic carbon burial flux of 5.5 x 10^{12} mol/yr, C:S ratios of ~1 (by mass), and a $^{34}\varepsilon_{global\_average}$ of -27‰. However, the model is relatively insensitive to the specific C:S ratio and value of $^{34}\varepsilon_{global\_average}$, because the combination of these two parameters together set seawater $\delta^{34}S_{SO4\text{-}sw}$ values. For example, models starting in steady state with a C:S wt. ratio of 2, require an $^{34}\varepsilon_{global\_average}$ value of -61‰ (or -55‰ for fully-coupled scenario) but the model calculates an almost identical $\delta^{34}S_{SO4\text{-}sw}$. This is because the decrease in pyrite burial flux does not affect the isotopic ratio of the output, as the pyrite that is buried has a significantly lighter isotopic composition. More realistic $^{34}\varepsilon_{global\_average}$ values of -37‰ (or -55‰ for fully-coupled scenario) with a C:S wt. ratio of 2 are achieved if the carbon input and burial fluxes are both increased by 50% (resulting in an organic carbon burial flux of 8.2 x 10^{12} mol/yr).

6.3.7. Sensitivity of the model to $^{34}\varepsilon_{SO4\text{-}pyr}$:

As mentioned in section 6.3.6 above, the model is relatively insensitive to the specific C:S ratio and value of $^{34}\varepsilon_{SO4\_pyr}$ because the combination of these two parameters together set seawater $\delta^{34}S_{SO4\text{-}sw}$ values. The value of $^{34}\varepsilon_{SO4\_pyr}$ is further split into a nearshore and a deep burial flux ($^{34}\varepsilon_{SO4\_pyr\_nearshore}$ and $^{34}\varepsilon_{SO4\_pyr\_deep}$, respectively), the relative proportion of the two fluxes being defined by f_{marine}, the fraction of deep pyrite burial to total burial.

In order to fully constrain the model and identify the most accurate estimate of average $^{34}\varepsilon_{SO4\_pyr\_nearshore}$ and $^{34}\varepsilon_{SO4\_pyr\_deep}$ values, a comprehensive and quantitative survey of modern sulfate-pyrite fractionation factors in different burial environments is needed. Our understanding of the range of fractionations and proportion of different environments in the Paleogene is even more sparse. In the absence of this

information, we have performed a sensitivity analysis on our model, to determine the range of reasonable values for $^{34}\varepsilon_{SO4\_pyr\_nearshore}$ and $^{34}\varepsilon_{SO4\_pyr\_deep}$ that can replicate the data. We ran model runs for a range of $^{34}\varepsilon_{SO4\_pyr\_nearshore}$ estimates from -3‰ to -20‰, for C:S ratios from 0.8 to 1.5. The model stated in steady state by varying $^{34}\varepsilon_{SO4\_pyr\_deep}$ and the initial f_{marine} (between -33‰ and -60‰, and between 60% and 80%, respectively). Model scenarios encompassing the full range of $^{34}\varepsilon_{SO4\_pyr\_nearshore}$ estimates fit the data, although when $^{34}\varepsilon_{SO4\_pyr\_nearshore}$ = -20‰, C:S ratios >1 are necessary for the initial f_{marine} to be greater than 60% (see Table S.3 for the range of values modelled that fit the data for $^{34}\varepsilon_{SO4\_pyr\_nearshore}$ values of -3, -5, -10, -15 and -20‰). The 5‰ increase in $\delta^{34}S_{SO4\text{-}sw}$ can be replicated at the centre of our estimated range for $^{34}\varepsilon_{SO4\_pyr\_nearshore}$, with an estimate of -10‰ for $^{34}\varepsilon_{SO4\_pyr\_nearshore,}$ a C:S ratio of 1, and an $^{34}\varepsilon_{SO4\_pyr\_deep}$ of -41.2‰, resulting in an initial $^{34}\varepsilon_{global\_average}$ of -31.4‰ when f_{marine} is 69%. $^{34}\varepsilon_{global\_average}$ then decreases by 9.8‰ to -41.2‰ as f_{marine} approaches 1. This is the model scenario that is described in the main text of the manuscript and shown in Figure 2 (red lines). The individual nearshore and deep pyrite burial fluxes are shown below in Figure S.20.

$^{34}\varepsilon_{SO4\_pyr\_nearshore}$ (‰)	$^{34}\varepsilon_{SO4\_pyr\_deep}$ (‰)	Initial f_{marine} (ramped over 0.5 Ma)	Initial $^{34}\varepsilon_{global\_average}$ (‰)	C:S
-3	-33.0	0.75	-25.1	0.8
-3	-41.2	0.75	-31.4	1
-3	-51.5	0.74	-39.2	1.25
-3	-61.8	0.74	-47.1	1.5
-5	-33.0	0.72	-25.1	0.8

-5	-41.2	0.73	-31.4	1
-5	-51.5	0.74	-39.2	1.25
-5	-61.8	0.74	-47.1	1.5
-10	-33.0	0.66	-25.1	0.8
-10	-41.2	0.69	-31.4	1
-10	-51.5	0.70	-39.2	1.25
-10	-61.8	0.72	-47.1	1.5
-15	-41.2	0.63	-31.4	1
-15	-51.5	0.66	-39.2	1.25
-15	-61.8	0.69	-47.1	1.5
-20	-51.5	0.61	-39.2	1.25
-20	-61.8	0.65	-47.1	1.5

Table S.3- (non-exclusive) range of parameters which fit the modelled data.

The model was also run for the fully coupled scenario, with the full range of $^{34}\varepsilon_{SO4\_pyr\_nearshore}$ estimates, although in this case f_{marine} was allowed to vary as low as 55%. A model run with C:S ratio of 1, $^{34}\varepsilon_{SO4\_pyr\_nearshore}$ of -10‰ and $^{34}\varepsilon_{SO4\_pyr\_deep}$ of -41.2‰, with an initial $^{34}\varepsilon_{global\_average}$ of -27.4‰ and an f_{marine} of 56% is also shown in Figures 2 and S.20 (black lines).

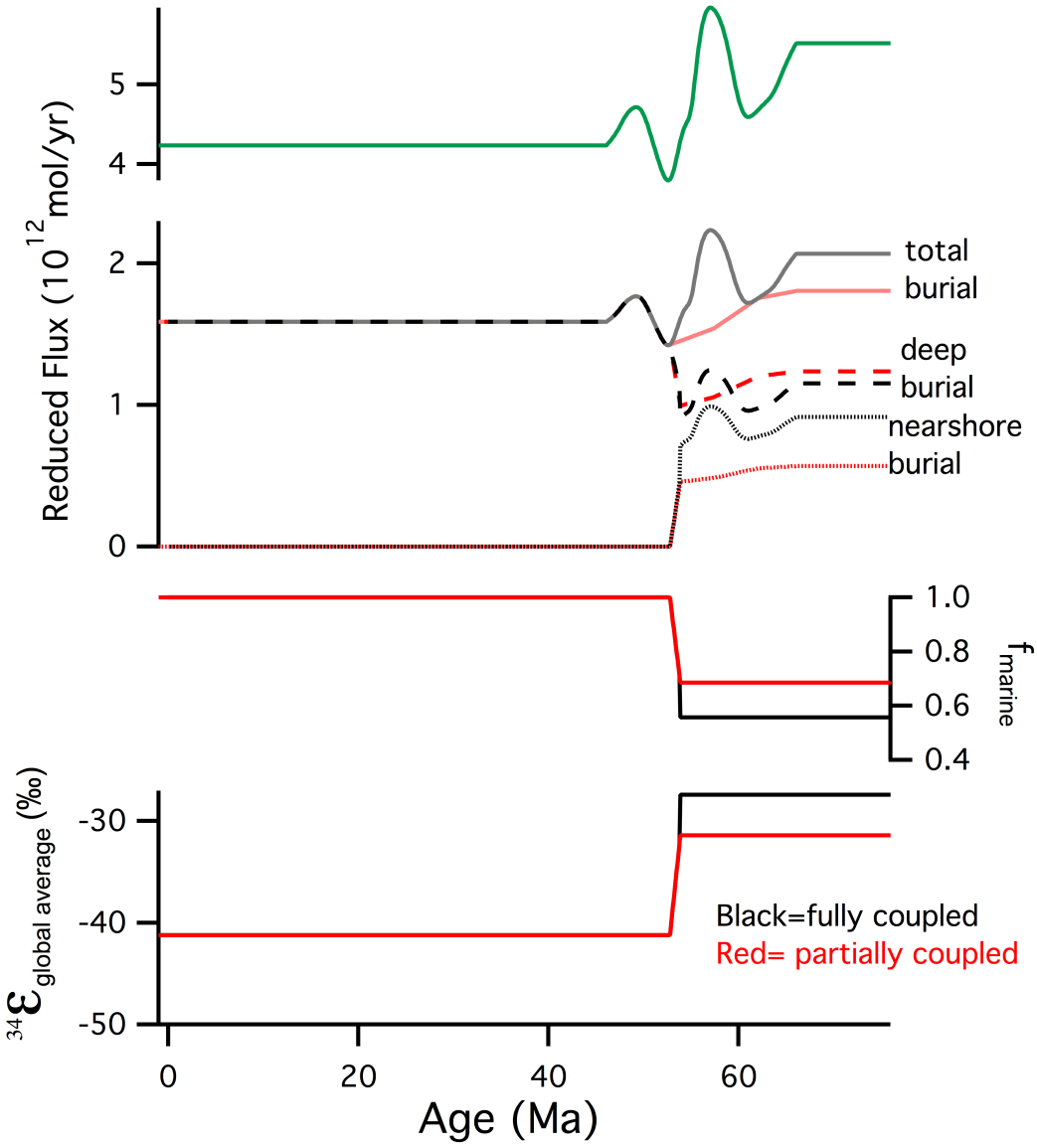

Figure S.20 –model input parameters for fully (black) and partially coupled (red) models. Organic carbon (green line) and total pyrite burial fluxes (solid lines) used as model input parameters. Pyrite burial fluxes are split into nearshore (dotted) and deep (dashed) burial fluxes by fmarine (the ratio of deep to total pyrite burial). The split fluxes sum to the total pyrite burial flux (solid lines). At 52.6 Ma, the deep pyrite burial flux converges onto the total pyrite burial flux, as nearshore burial is suppressed.

$^{34}\varepsilon_{global\_average}$ is the sum of $^{34}\varepsilon_{SO4\_pyr\_nearshore}$ and $^{34}\varepsilon_{SO4\_pyr\_deep}$, weighted by deep/total pyrite burial (which for these runs is initially 70% (partially-coupled), and 55% (fully-coupled)). C:S=1, evaporite burial flux=1.4×10^{12} (coupled), and 1.7×10^{12} (partially coupled) mol/yr.

6.3.8. Sensitivity of the model to pyrite burial assumptions:

The term f_{marine}, has been parameterized such that the loss of pyrite burial in epicratonic seas is matched by an increase in pyrite burial in the deep ocean, as f_{marine} varies from ~0.7 to 1 (see equations S.11 and S.12). We assume this because in the modern ocean, the dominant supply of iron will be from terrestrial weathering and from hydrothermal input. Because iron is soluble only in its reduced form, iron oxides will form and will settle in the ocean; within sediments they will be reduced to ferrous iron, which is then available to precipitate with sulfide as pyrite. Iron delivery to sediments will therefore be concentrated near hydrothermal systems (where microbial sulfate reduction rates are low, and therefore pyrite burial may be lower) and near land through riverine input. If we consider that iron delivery extends a certain distance out from a marginal marine environment, then where sealevel hits the hypsometric distribution of land will be key for the distribution of pyrite burial and, importantly, its sulfur isotopic composition. It may be, however, that the change in the locus of pyrite burial also pushes sulfide production into zones where iron does not reach, and therefore pyrite burial rates may actually decrease across the interval where the $\delta^{34}S$ of seawater sulfate increases. In this case the model equations are rewritten as follows:

$$V_{Ocean} \times \frac{\partial[^{32}S]}{\partial t} = F_{W\,^{32}S} - f_{marine\_0} \times F_{red^{32}S} - (1 - f_{marine}) \times F_{red^{32}S} - F_{evap^{32}} \quad \text{(S.13)}$$

$$V_{Ocean} \times \frac{\partial[^{34}S]}{\partial t} = F_{W\,^{32}S} \times {}^{34}R_{in} - f_{marine\_0} \times F_{red\,^{32}S} \left(\frac{\delta^{34}S_{ocean} + \varepsilon_{SO4\_pyr\_deep}}{1000} + 1 \right) \times {}^{34}R_S - (1 - f_{marine}) \times F_{red\,^{32}S} \left(\frac{\delta^{34}S_{ocean} + \varepsilon_{SO4\_pyr\_nearshore}}{1000} + 1 \right) \times {}^{34}R_S - F_{evap\,^{32}} \times {}^{34}R_{ocean} \quad \text{(S.14)}$$

Where f_{marine_0} is the initial ratio of marine to epicratonic burial.

Solutions to this model version that replicate the data require that $^{34}\varepsilon_{global\ aveage}$ of this pyrite must decrease by an even larger amount (by a further 12.5‰ – to -47.9‰ in the case of model run 6.3.3 (C:S= 0.86, initial $^{34}\varepsilon_{global\_average}$ = -27‰), which is still within the range of reported fractionations).

References

1 Angell, R. W. Test morphogenesis (chamber formation) in the foraminifer Spiroloculina hyalina Schulze. *The Journal of Foraminiferal Research* **10**, 89-101 (1980).

2 Paris, G., Fehrenbacher, J. S., Sessions, A. L., Spero, H. J. & Adkins, J. F. Experimental determination of carbonate‐associated sulfate δ34S in planktonic foraminifera shells. *Geochemistry, Geophysics, Geosystems* **15**, 1452-1461 (2014).

3 Rosenthal, Y., Boyle, E. A. & Slowey, N. Temperature control on the incorporation of magnesium, strontium, fluorine, and cadmium into benthic

foraminiferal shells from Little Bahama Bank: Prospects for thermocline paleoceanography. *Geochim Cosmochim Ac* **61**, 3633-3643 (1997).

4 Barker, S., Greaves, M. & Elderfield, H. A study of cleaning procedures used for foraminiferal Mg/Ca paleothermometry. *Geochemistry, Geophysics, Geosystems* **4** (2003).

5 Lea, D. W. & Boyle, E. A. Barium in planktonic foraminifera. *Geochim Cosmochim Ac* **55**, 3321-3331 (1991).

6 Present, T. M., Paris, G., Burke, A., Fischer, W. W. & Adkins, J. F. Large Carbonate Associated Sulfate isotopic variability between brachiopods, micrite, and other sedimentary components in Late Ordovician strata. *Earth Planet Sc Lett* **432**, 187-198, doi:https://doi.org/10.1016/j.epsl.2015.10.005 (2015).

7 Marenco, P. J., Corsetti, F. A., Hammond, D. E., Kaufman, A. J. & Bottjer, D. J. Oxidation of pyrite during extraction of carbonate associated sulfate. *Chem Geol* **247**, 124-132 (2008).

8 Boyle, E. A. Cadmium, zinc, copper, and barium in foraminifera tests. *Earth Planet Sc Lett* **53**, 11-35 (1981).

9 Paris, G., Fehrenbacher, J. S., Sessions, A. L., Spero, H. J. & Adkins, J. F. Experimental determination of carbonate-associated sulfate delta S-34 in planktonic foraminifera shells. *Geochem Geophy Geosy* **15**, 1452-1461, doi:Doi 10.1002/2014gc005295 (2014).

10 Paris, G., Sessions, A. L., Subhas, A. V. & Adkins, J. F. MC-ICP-MS measurement of delta S-34 and Delta S-33 in small amounts of dissolved sulfate. *Chem Geol* **345**, 50-61, doi:Doi 10.1016/J.Chemgeo.2013.02.022 (2013).

11 Kump, L. R. & Garrels, R. M. Modeling Atmospheric O-2 in the Global Sedimentary Redox Cycle. *Am J Sci* **286**, 337-360 (1986).

12 Mazumdar, A., Goldberg, T. & Strauss, H. Abiotic oxidation of pyrite by Fe (III) in acidic media and its implications for sulfur isotope measurements of lattice-bound sulfate in sediments. *Chem Geol* **253**, 30-37 (2008).

13 Hodell, D. A. *et al.* Variations in the strontium isotope composition of seawater during the Paleocene and early Eocene from ODP Leg 208 (Walvis Ridge). *Geochem Geophy Geosy* **8**, doi:Artn Q09001 Doi 10.1029/2007gc001607 (2007).

14 Zachos, J. C. & al, e. *Proceedings of the Ocean Drilling Program Initial Report*. Vol. 208 (Ocean Drill. Program, 2004).

15 Hodell, D. A., Mueller, P. A. & Garrido, J. R. Variations in the Strontium Isotopic Composition of Seawater during the Neogene. *Geology* **19**, 24-27, doi:Doi 10.1130/0091-7613(1991)019<0024:Vitsic>2.3.Co;2 (1991).

16 Martin, E. E., Shackleton, N. J., Zachos, J. C. & Flower, B. P. Orbitally-tuned Sr isotope chemostratigraphy for the late middle to late Miocene. *Paleoceanography* **14**, 74-83, doi:Doi 10.1029/1998pa900008 (1999).

17 Martin, E. E. & Scher, H. D. Preservation of seawater Sr and Nd isotopes in fossil fish teeth: bad news and good news. *Earth Planet Sc Lett* **220**, 25-39, doi:10.1016/S0012-821x(04)00030-5 (2004).

18 Farrell, J. W., Clemens, S. C. & Gromet, L. P. Improved Chronostratigraphic Reference Curve of Late Neogene Seawater Sr-87/Sr-86. *Geology* **23**, 403-406, doi:Doi 10.1130/0091-7613(1995)023<0403:Icrcol>2.3.Co;2 (1995).

19 Westerhold, T. *et al.* Astronomical calibration of the Paleocene time. *Palaeogeography, Palaeoclimatology, Palaeoecology* **257**, 377-403 (2008).

20 Zachos, J. C., Dickens, G. R. & Zeebe, R. E. An early Cenozoic perspective on greenhouse warming and carbon-cycle dynamics. *Nature* **451**, 279-283, doi:Doi 10.1038/Nature06588 (2008).
21 Kurtz, A. C., Kump, L. R., Arthur, M. A., Zachos, J. C. & Paytan, A. Early Cenozoic decoupling of the global carbon and sulfur cycles. *Paleoceanography* **18** (2003).
22 Paytan, A., Kastner, M., Campbell, D. & Thiemens, M. H. Sulfur isotopic composition of Cenozoic seawater sulfate. *Science* **282**, 1459-1462, doi:Doi 10.1126/Science.282.5393.1459 (1998).
23 Halevy, I., Peters, S. E. & Fischer, W. W. Sulfate Burial Constraints on the Phanerozoic Sulfur Cycle. *Science* **337**, 331-334, doi:10.1126/science.1220224 (2012).
24 Ding, T. *et al.* Calibrated sulfur isotope abundance ratios of three IAEA sulfur isotope reference materials and V-CDT with a reassessment of the atomic weight of sulfur. *Geochim Cosmochim Ac* **65**, 2433-2437, doi:https://doi.org/10.1016/S0016-7037(01)00611-1 (2001).
25 Zeebe, R. E. & Wolf-Gladrow, D. *CO2 in Seawater: Equilibrium, Kinetics, Isotopes.*, (2001).
26 Komar, N., Zeebe, R. & Dickens, G. Understanding long‐term carbon cycle trends: The late Paleocene through the early Eocene. *Paleoceanography* **28**, 650-662 (2013).
27 Hayes, J. M. & Waldbauer, J. R. The carbon cycle and associated redox processes through time. *Philosophical Transactions of the Royal Society B: Biological Sciences* **361**, 931-950, doi:10.1098/rstb.2006.1840 (2006).
28 Marais, D. J. D., Strauss, H., Summons, R. E. & Hayes, J. M. Carbon isotope evidence for the stepwise oxidation of the Proterozoic environment. *Nature* **359**, 605, doi:10.1038/359605a0 (1992).
29 Macko, S. A. & Pereira, C. P. 50. NEOGENE PALEOCLIMATE DEVELOPMENT OF THE ANTARCTIC WEDDELL SEA REGION: ORGANIC GEOCHEMISTRY1.
30 Hayes, J. M., Strauss, H. & Kaufman, A. J. The abundance of 13C in marine organic matter and isotopic fractionation in the global biogeochemical cycle of carbon during the past 800 Ma. *Chem Geol* **161**, 103-125, doi:https://doi.org/10.1016/S0009-2541(99)00083-2 (1999).
31 McCorkle, D. C., Corliss, B. H. & Farnham, C. A. Vertical distributions and stable isotopic compositions of live (stained) benthic foraminifera from the North Carolina and California continental margins. *Deep Sea Research Part I: Oceanographic Research Papers* **44**, 983-1024 (1997).
32 Reinsch, C. H. Smoothing by Spline Functions. *Numerische Mathematic* **10**, 177-183 (1967).
33 Canfield, D. E. The evolution of the Earth surface sulfur reservoir. *Am J Sci* **304**, 839-861, doi:DOI 10.2475/ajs.304.10.839 (2004).
34 Holser, W. T., Schidlowski, M., Mackenzie, F. T. & Maynard, J. B. *Chemical Cycles in the Evolution of the Earth*. 105-173 (Wiley, 1988).
35 Canfield, D. E. Sulfur isotopes in coal constrain the evolution of the Phanerozoic sulfur cycle. *P Natl Acad Sci USA* **110**, 8443-8446, doi:10.1073/pnas.1306450110 (2013).
36 Berresheim, H. & Jaeschke, W. The Contribution of Volcanos to the Global Atmospheric Sulfur Budget. *J Geophys Res-Oc Atm* **88**, 3732-3740, doi:DOI 10.1029/JC088iC06p03732 (1983).

37 Horita, J., Zimmermann, H. & Holland, H. D. Chemical evolution of seawater during the Phanerozoic: Implications from the record of marine evaporites. *Geochim Cosmochim Ac* **66**, 3733-3756, doi:Pii S0016-7037(01)00884-5 Doi 10.1016/S0016-7037(01)00884-5 (2002).
38 Alt, J. C. *et al.* The role of serpentinites in cycling of carbon and sulfur: Seafloor serpentinization and subduction metamorphism. *Lithos* **178**, 40-54, doi:10.1016/j.lithos.2012.12.006 (2013).
39 Burke, A. *et al.* in *Goldschmidt Abstracts* 427 (2015).
40 Turchyn, A. V. & Schrag, D. P. Oxygen isotope constraints on the sulfur cycle over the past 10 million years. *Science* **303**, 2004-2007, doi:DOI 10.1126/science.1092296 (2004).
41 D'Hondt, S., Rutherford, S. & Spivack, A. J. Metabolic activity of subsurface life in deep-sea sediments. *Science* **295**, 2067-2070, doi:DOI 10.1126/science.1064878 (2002).
42 Jorgensen, B. B. Mineralization of Organic-Matter in the Sea Bed - the Role of Sulfate Reduction. *Nature* **296**, 643-645, doi:DOI 10.1038/296643a0 (1982).
43 Canfield, D. E. Sulfate Reduction in Deep-Sea Sediments. *Am J Sci* **291**, 177-188 (1991).
44 Bottrell, S. H., Parkes, R. J., Cragg, B. A. & Raiswell, R. Isotopic evidence for anoxic pyrite oxidation and stimulation of bacterial sulphate reduction in marine sediments. *J Geol Soc London* **157**, 711-714 (2000).
45 Ono, S., Wing, B., Rumble, D. & Farquhar, J. High precision analysis of all four stable isotopes of sulfur (S-32, S-33, S-34 and S-36) at nanomole levels using a laser fluorination isotope-ratio-monitoring gas chromatography-mass spectrometry. *Chem Geol* **225**, 30-39, doi:10.1016/j.chemgeo.2005.08.005 (2006).
46 Tostevin, R. *et al.* Multiple sulfur isotope constraints on the modern sulfur cycle. *Earth Planet Sc Lett* **396**, 14-21, doi:10.1016/j.epsl.2014.03.057 (2014).
47 Holser, W. T., Kaplan, I. R., Sakai, H. & Zak, I. Isotope Geochemistry of Oxygen in the Sedimentary Sulfate Cycle. *Chem Geol* **25**, 1-17, doi:Doi 10.1016/0009-2541(79)90079-2 (1979).
48 Raab, M. & Spiro, B. Sulfur Isotopic Variations during Seawater Evaporation with Fractional Crystallization. *Chem Geol* **86**, 323-333, doi:Doi 10.1016/0168-9622(91)90014-N (1991).
49 Holser, W. T. Trace elements and isotopes in evaporites. *Reviews in Mineralogy* **6** (1979).
50 Raiswell, R., Whaler, K., Dean, S., Coleman, M. L. & Briggs, D. E. G. A Simple 3-Dimensional Model of Diffusion-with-Precipitation Applied to Localized Pyrite Formation in Framboids, Fossils and Detrital Iron Minerals. *Mar Geol* **113**, 89-100, doi:Doi 10.1016/0025-3227(93)90151-K (1993).
51 Higgins, J. A. & Schrag, D. P. Beyond methane: Towards a theory for the Paleocene-Eocene Thermal Maximum. *Earth Planet Sc Lett* **245**, 523-537, doi:Doi 10.1016/J.Epsl.2006.03.009 (2006).